GEOMETRY INDUCED FLOW DISTURBANCES

Saami K. Yazdani

A thesis submitted to the Faculty of the Virginia Polytechnic Institute and State University in partial fulfillment of the requirements for the degree of

Master of Science

in

Engineering Mechanics

Approved by

Dr. Pavlos Vlachos, Chairperson of Supervisor Committee
Dr. Demetri Telionis
Dr. Joel Berry

September 19, 2003
Blacksburg, Virginia

Keywords: Stent, Bifurcation, DPIV, Flow Separation, Vortex

ABSTRACT

Saami K. Yazdani

Geometry Induced Flow Disturbances

From clinical studies it is well known that atherosclerosis has preferred locations in the vascular system, primarily sited in the carotid arteries, coronary arteries, and in vessels supplying the lower extremities in the arterial system. In the vicinity of bifurcations flow tends to separate forming re-circulation regions. In addition, due to the pulsatile character of blood flow during the deceleration part of the cycle, the flow becomes unstable and transition to turbulence may occur. Vascular stents provide a novel method in treatment of atherosclerotic vessels. Although stents have dramatically decreased the re-stenosis rate of vessels compared to balloon-angioplasty, restenosis still occurs in 25-30% of coronary implanted stents. Understanding how stents influence flow patterns may lead to more hemodynamically compatible stent designs that alleviate thrombus formation and promote endothelialization.

The first study employed time-resolved Digital Particle Image Velocimetry (DPIV) to compare the hemodynamic performance of two stents in a compliant vessel. The first stent was a rigid insert, representing an extreme compliance mismatch. The second stent was a commercially available nitinol stent with some flexural characteristics. DPIV showed that compliance mismatch promotes the formation of a ring vortex in the vicinity of the stent. Larger compliance mismatch increased both the size and residence time of the ring vortex, and introduced in-flow stagnation points. These results provide detailed quantitative evidence of the hemodynamic effect of stent mechanical properties. Better understanding of these characteristics will provide valuable information for modifying stent design in order to promote long-term

In the second study, DPIV was utilized to explore the fluid dynamics phenomena in a symmetric compliant bifurcation. We studied the effects of the Womersley and the Reynolds numbers under pulsatile flow conditions. New insight of the fluid mechanics

is revealed. The flow topology results indicate that the formation of coherent vortices in the vicinity of the bifurcation apex is governed by physical process that dictates the energy and strength of the formed vortices. This is manifested by the identification of a characteristic dimensionless time-scale that combines the impulsive vortex formation with the inertia of the unsteady flow.

TABLE OF CONTENTS

LIST OF FIGURES

LIST OF TABLES

Aknowledgments

I would like to thank all the members of my committee. Dr. Demetri Telionis, your doors have always been open to me for any question, guidance, and helpful insights to the world of fluids. I truly enjoyed setting in your office and learning the fundamentals. Dr. Joel Berry, you have open new doors for me and I am very thankful. I want to thank you for supporting me in my last year of my Masters program. Your knowledge in biology has been very helpful in our research efforts at Virginia Tech. Your balance in life and academia is inspiring. Dr. Pavlos Vlachos, I am indebted to your assistance in the last few years. You have been the coach that knew exactly what buttons to push to get the best out of me. Although I might have not reached all the expectations you had for me, I recognize that your expectations reflect your high regards to my abilities and I am thankful for that.

I would also like to thank my co-graduate students. Olga Pierrakos, you have been a great friend and a helpful resource. Ali Etebari, your willingness to help in any situation is regarded very highly from me. John Charonko, your studios ways have helped me and the lab in more ways than you can imagine. Robert Hodges, your expertise in electronics and circuits has helped me in all of my research and experiments.

Lastly, I would like to thank my family and Diana. Dad, thanks for supporting me in all of my college years. I will pay you back one day, I promise. Arrash, you are the best brother anyone could have. I love you dearly. Diana, I would like to thank you for all your support. I know if was not ideal situation to keep me company until 1 a.m. on numerous nights in the fluids lab. I am truly grateful for your patient, love, and flexibility.

Chapter 1

DPIV Measurements of Flow Disturbances in Stented Artery Model: Adverse Effects of Compliance Mismatch

1.1. Introduction

The use of stents has dramatically increased since their approval by the United States Food and Drug Administration in 1994, largely as a result of technological advances. The clinical success of stenting has been due to their therapeutic advantage over balloon angioplasty alone despite the persistent problem of in-stent restenosis. Most recently, stents coated with antimitotic agents have shown promising results with extremely low rates of clinical events over the short and mid-term. Small sample sizes, careful patient selection and short follow-up periods remain important limitations of these results [1].

Although existing stents perform their function of supporting diseased arterial tissue, stent design profoundly influences the post-procedural hemodynamic and solid mechanical environment of the stented artery [2,3,4]. This alteration in the mechanical environment is emerging as an important factor in the long-term patency of stented vessels. Both in vitro and in vivo studies have revealed that stent structure influences global [2] and local [5] flow patterns, thrombus accumulation between struts [6], and restenosis [7]. Recently, coronary restenosis in patients receiving a variety of stent types was shown to be most dependent on vessel size and stent design [8]. Tominaga et al. [4] implanted spiral Nitinol stents in rabbit aortas and measured significantly less neointima formation in the stents that had gaps between the struts. Moreover, the pattern of accumulation appeared similar to the zones of flow stagnation predicted upstream and downstream of stent struts using computational fluid dynamics [5]. Rogers and Edelman [7] reported significantly less neointimal hyperplasia in balloon expandable stent designs fabricated with reduced strut-strut intersections

The evidence implicating specific flow patterns in atherogenesis and vascular graft failure is potentially relevant to stent failure. Fluid dynamics studies in the human aorta [9], carotid arteries [10] and coronary arteries [11] have yielded a strong correlation between intimal thickening and specific flow patterns occurring at focal

locations in these vessels. Low mean shear stress, oscillating shear stress, high particle residence times and non-laminar flow have all been shown to occur in the locations where early intimal thickening is greatest. Studies in both end-to-side and end-to-end anastomotic geometries have indicated that similar flow patterns are found in the specific areas where vascular grafts are known to develop stenoses. Compliance mismatch between vascular graft and host vessel is implicated as a culprit in neointimal hyperplasia [12,13,14,15,16,17]. One of the consequences of compliance mismatch in a vessel is local blood flow alteration [15]. Low mean shear rates and flow stagnation is correlated with intimal thickening. Many of these same fluid dynamic features have been reported in models of stented vessels.

This study was undertaken to examine the effects of compliance mismatched and compliance matched stents in a straight tube model subjected to pulsatile flow using Digital Particle Image Velocimetry (DPIV). The ability of DPIV to discern secondary flow patterns is exploited here to determine the effects of stent design on the development of non-laminar flow patterns.

1.2. Methods

1.2.1. Experimental Setup

The experimental setup was comprised of a computer controlled gear pump (Ismatec Inc., Glattburgg, Switzerland, drive 'MV-Z' with micropump pumphead model 201) connected to a compliant 30 cm long straight transparent vessel. The tube was contained in an acrylic box submerged with the working fluid in order to allow for optical access and account for index of refraction distortions. The working fluid was an equal mixture of water and glycerin (ρ = 1.13 g/cm^3, ν = 5.55e-2 cm^2/sec). Two intravascular pressure transducers (Millar Instruments, Inc. Houston, TX, model no. SPC-330A) were inserted proximal and distal to the stent site recording the instantaneous pressure. Upstream and downstream flow rates were measured with two ultrasonic flow meters (Transonic Systems Inc., Ithaca, NY, Model T110) with a 30 Hz frequency response. An 8-channel, 16-bit, 1MHz (CIO-DAS16/M1/16) data acquisition board was used for the digital to analog conversion and data recording.

Data were taken with a frequency of a 1000 Hz for a period of 4 seconds. A schematic representation of the experimental setup is presented in Fig. 1.1.

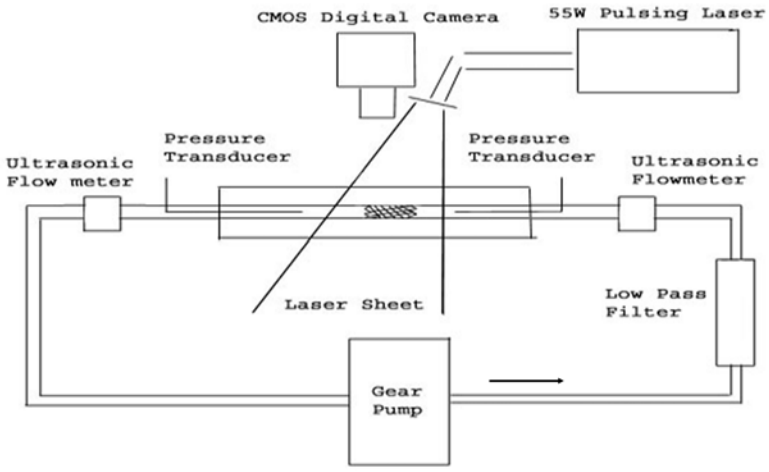

Figure 1.1: Schematic of experimental setup used to perform DPIV. The arrow indicates direction of flow.

1.2.2. Vessel and Stent Compliance

The vessel hosting the stent was constructed from a transparent elastomeric silicone (Sylgard 184, Dow Corning Corporation, Midland, MI) 12 mm inner diameter with a 0.5 mm wall thickness. More details can be found from previous publications on fabrication and specification of these vessels [2]. To compare and study the effects of compliance mismatch, two stents were used. The first was a transparent rigid cylinder and the second was a Cordis Smart Stent (Cordis Corporation, a Johnson & Johnson Company, Warren, NJ). The Smart stent was fabricated from the shape memory metal called nitinol and was more elastic than the rigid cylinder but stiffer than the host vessel. Figure 1.2 illustrates the diameter compliance of both the vessel and vessel-stent compliance. The zero position of Fig. 1.2 represents the leading edge of the stent. The rigid cylinder and the SMART stent were 13 mm in diameter uncompressed. The thickness of the rigid cylinder was 0.55 mm, 4% of the overall diameter. The thickness of the SMART stent was 0.145 mm, 1% of the overall diameter. Both Stents were 25 mm in length.

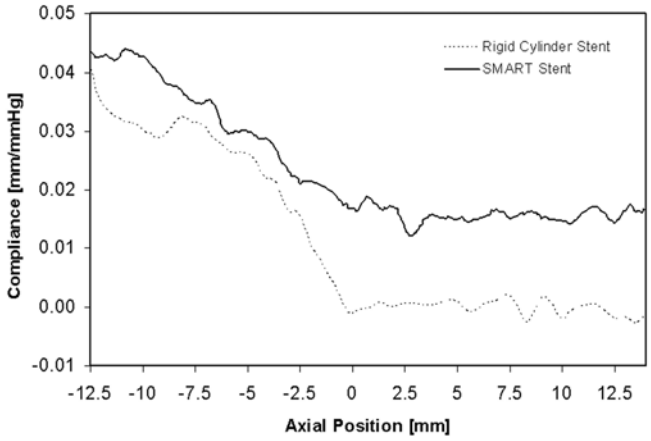

Figure 1.2: Diameter compliance measurements of both the SMART and solid cylinder stent. The zero position represents the leading edge of the stent. The solid line represents the SMART stent-vessel compliance. The dashed line represents the solid cylinder stent-vessel compliance.

1.2.3. Flow Waveform

The flow conditions generated corresponded to in vivo exercise conditions dynamically scaled according to the Reynolds number, Re, and Womersley parameter, α. The Reynolds number represents the ratio of the inertial forces over the viscous forces and was determined from the relation

$$\mathrm{Re} = \frac{UL}{\nu} = \frac{4Q}{\pi \nu d}$$

where U is the average fluid velocity, L is a characteristic length (vessel diameter), Q is time-averaged volume flow rate, ν is the kinematic viscosity of the fluid and d is the diameter of the vessel. The Womersley parameter is the ratio of unsteady forces to viscous forces and was determined from the relation

$$\alpha = \frac{d}{2}\sqrt{\frac{w}{\nu}}$$

where d is the tube diameter and w is the pulse rate in radians per second. For this study, the mean Reynolds number used was 300 (466 ml/min), the peak Reynolds number was 1250 (1940 ml/min), and the Womersley parameter was 4.89 (90

beats/min). The measured flow rate waveform is shown in Fig. 1.3. Pressure ranged from 85-120 mmHg corresponding to physiological conditions.

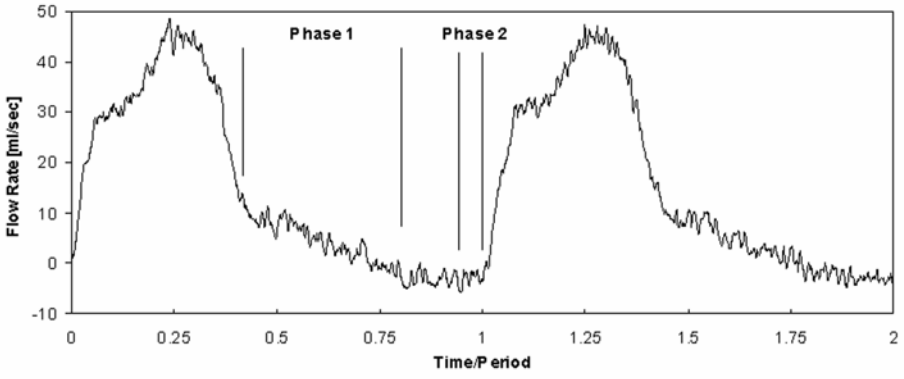

Figure 1.3: Measured Flow Waveform via ultrasonic flow meters located upstream of test section. Location of the two phases investigated in the pulsatile cycle. Phase 1 corresponded to 0.4 to 0.8 T (T: period of the pulse). Phase 2 corresponded to 0.95 to 1.0 T.

1.2.4. DPIV System Details

A pulsing laser beam (55Watts) was guided through a series of mirrors and lenses in order to form a 2 mm thick laser sheet that illuminated the planar area of interrogation. Area of interrogation was approximately 1 diameter upstream and 1diameter downstream of the leading edge of the stent. Neutrally buoyant fluorescent particles (J. H. Engineering, Baltimore MD) were used as flow tracers in the working fluid (a glycerin/water mixture). The particle diameters were approximately 30 microns to insure that they accurately followed the path of the flow with limited response lag to velocity fluctuations. A fast CMOS digital camera (1000 frames/sec) was used to record the instantaneous positions of the particles. The recorded images were processed to evaluate the instantaneous velocity fields by applying a dual frame dynamically adaptive multigrid cross-correlation scheme [18,19]. The accuracy of the method is independent of the velocity gradients and the rotationality of the flow and delivers superior spatial resolution compared with conventional methods. For the conditions of the present experiments the accuracy was estimated to be approximately 0.05 pixels with a velocity vector grid spacing of 266 microns. The camera and D/A

board were synchronized resulting in simultaneous pressure, flow rate measurements and DPIV data.

1.3. Results

The character of the flow in a stented region is governed by the flow waveform, pulsatility, and the compliance mismatch. Vortex formation has been shown to originate from stent compliance mismatch in a pulsatile flow field [2]. To better examine the temporal and spatial evolution of these vortices, we are presenting DPIV results using instantaneous streamlines, lines tangent to the local velocity vectors. Pulsatile flow in a straight vessel tends to be inherently unstable during the deceleration phase of the pulse cycle, possibly creating separation and vortical structures. Thus our analysis focused on the two phases that corresponded to the unstable part of the cycle. Phase 1 occurred during the time-period of 0.4 to 0.8 T (T: period of the pulse) where the decelerating flow began to separate and fully reverse. This corresponded to the interval between late systole and early diastole (Fig. 1.3). Subsequently, phase 2 occurred during time-period of 0.95 to 1.0 T where the reverse flow ceased and forward flow ensued again (late diastole to early systole, Fig. 1.3). We note that high frequency fluctuations present in the flow waveform are a result of transducer noise inherent in the signal.

Vortical formation throughout phase 1 of the SMART stent is shown in Fig. 1.4. The horizontal black line (Y/D = 0) in each frame represents the leading edge of the stent and our field of view is limited to approximately 1 diameter upstream and downstream of the stent. The time intervals between the consecutive instantaneous flow fields presented here are 0.05 seconds. The direction of flow is from top to bottom. As flow decelerates through the stented vessel, an unsteady shear layer grows upwards (opposite of the main flow) indicated by the streamlines deviated from the vessel walls (Fig. 1.4a). In the vicinity of the leading edge of the stent, the shear layer begins to destabilize and begins to roll in a spiral motion resembling a vortex (Fig. 4b and 4c). As time progresses, the spiral structure evolves into a clockwise rotating vortical structure with its locus position approximately at 0.35 X/D and –0.4 Y/D (Fig. 1.4f). A second counter-rotating vortex is observed at 0 Y/D and 0.75 X/D. These two counter-rotating vortices interact and migrate towards the center (Fig. 1.4g) and

then diffuse into the flow (Fig. 1.4h). Thus, the development of vortices dominates the flow field in the SMART stent during phase 1.

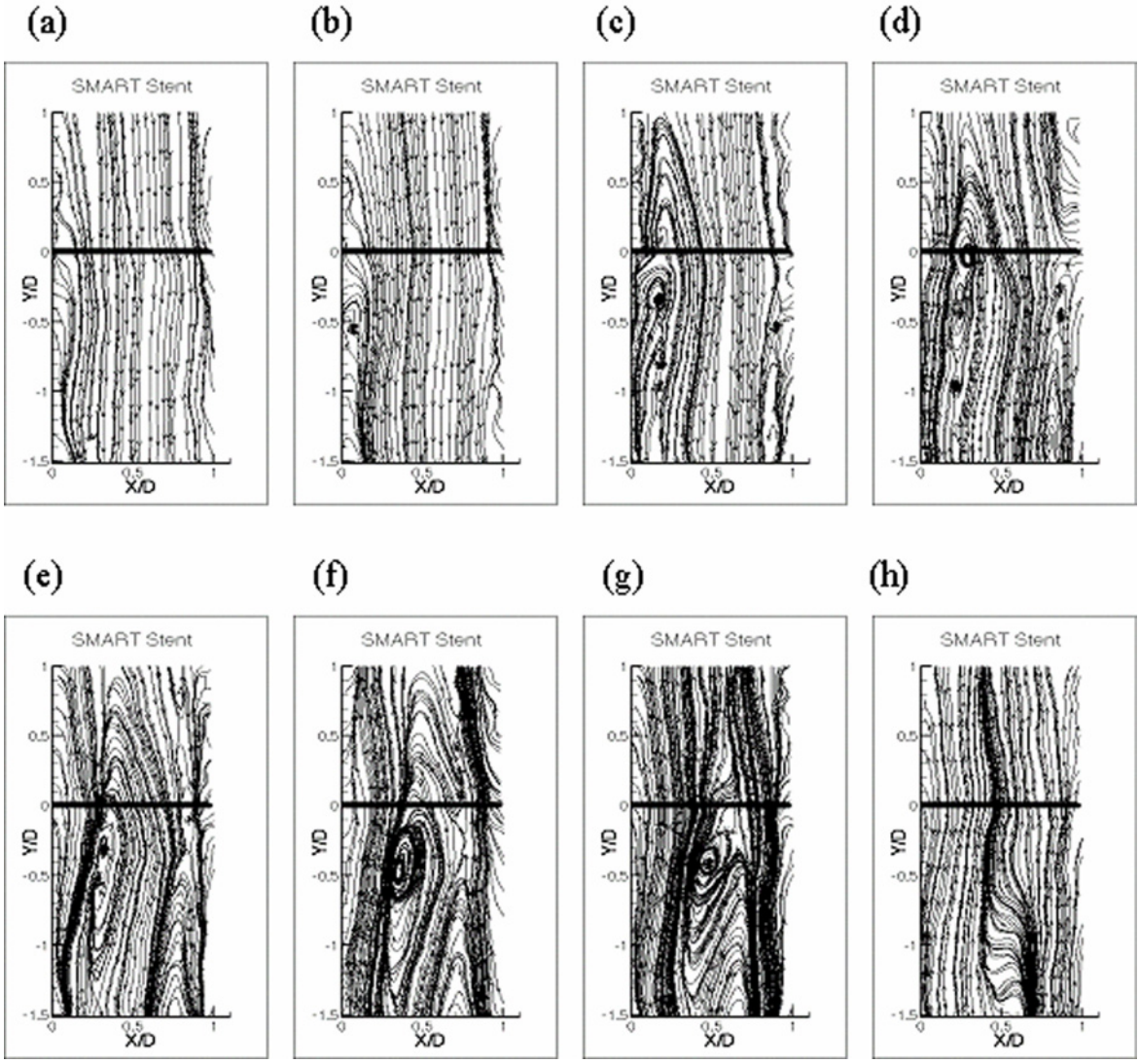

Figure 1.4: Flow development during phase 1 of the SMART stent illustrated via streamlines. As flow begins to decelerate, a propagating unsteady shear layer is shown to develop opposing the main flow (flow is from top to bottom). The shear layer detaches from the wall and rolls into a clockwise vortical structure near the leading edge of the stent. As flow fully reverses, the vortex is diffused into the flow.

Similar patterns may be seen for phase 1 of the rigid cylinder stent in Fig. 1.5. As the flow decelerates, an unsteady shear layer begins to form (Fig. 1.5a). Figure 1.5b shows the formation of a clockwise rotating vortical structure in the vicinity of the leading edge of the rigid cylinder stent at -0.2 Y/D and 0 X/D. Similar to the SMART

stent, a second counter rotating vortical structure can be observed in Fig. 1.5c. These two counter-rotating vortices imply the existence of a ring vortex, as explained below in the discussion section. Figures 1.5b through Fig. 1.5e illustrate the ring vortex (two counter-rotating vortices) remained in the vicinity of the vessel wall for approximately 0.04 seconds. Creation of secondary vortices on the vessel walls initiates the migration of the ring vortex toward the center of the vessel (Fig. 1.5e through Fig. 1.5f). As the ring vortex migrates toward the center, it diffuses into the flow (Fig 1.5g and Fig. 1.5h). In a manner similar to the SMART stent, coherent vortices also dominate the flow field in the rigid cylinder stent, although the observed vortices are 100% longer in resident time and are 100% larger in size.

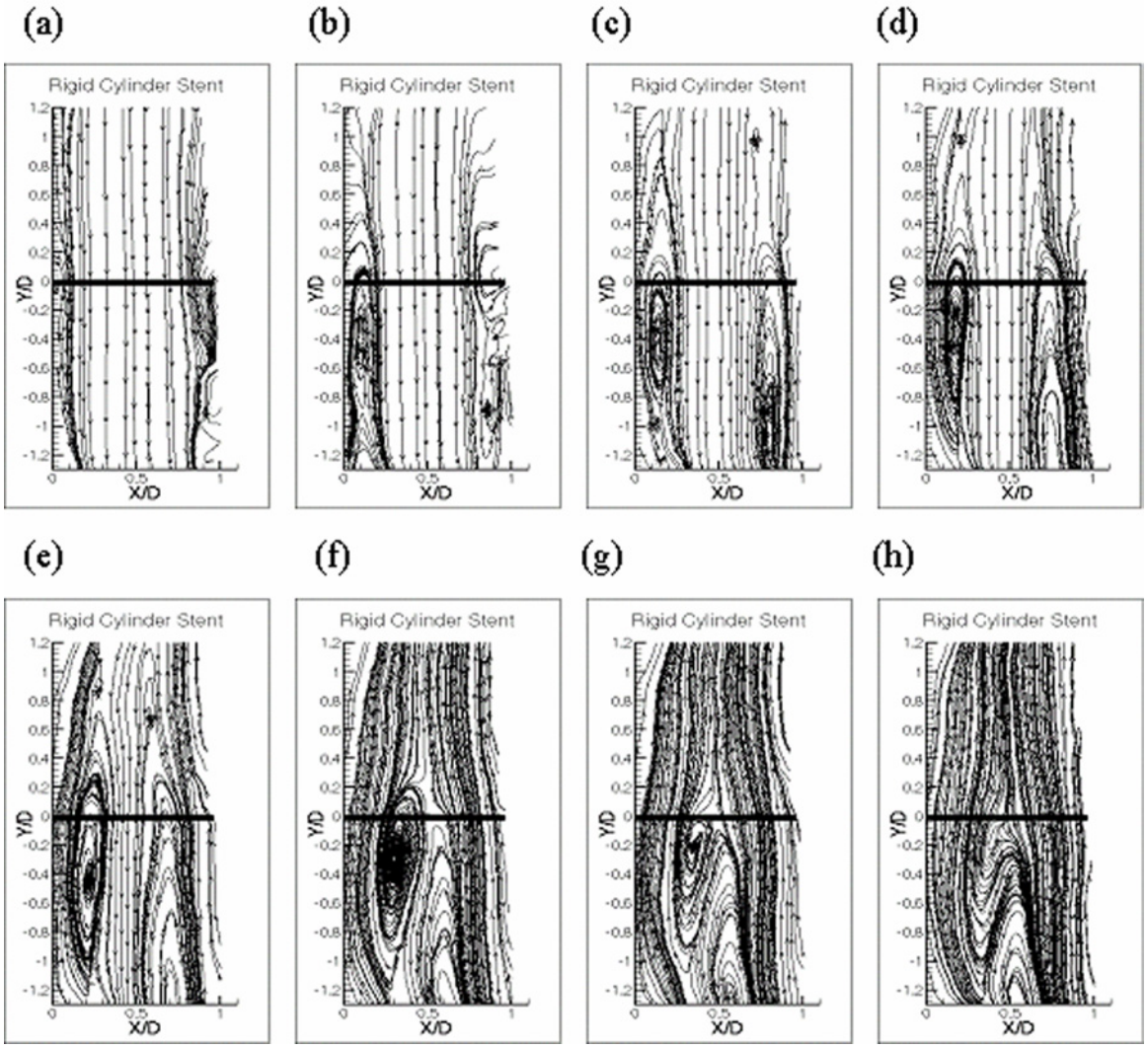

Figure 1.5: Flow development during phase 1 of the solid cylinder stent as illustrated via streamlines. As flow begins to decelerate, a propagating unsteady shear layer is shown to develop opposing the main flow (flow is from top to bottom). The shear layer detaches from the wall and rolls into a clockwise vortical structure near the leading edge of the stent. As flow fully reverses, the vortex is diffused into the flow.

Figure 1.6 illustrates the flow behavior during late diastole/early systole (phase 2) of the SMART stent. Unlike phase 1, the time interval between each image is 0.005 sec. The transition time measured between reverse flow and forward flow was approximately 0.03 seconds. A symmetric flow behavior was observed in Fig. 1.6b through Fig. 1.6d. Within the duration of phase 2 for the SMART stent, the change of

direction of the flow, from reverse to forward is not associated with the formation of coherent vortical structures.

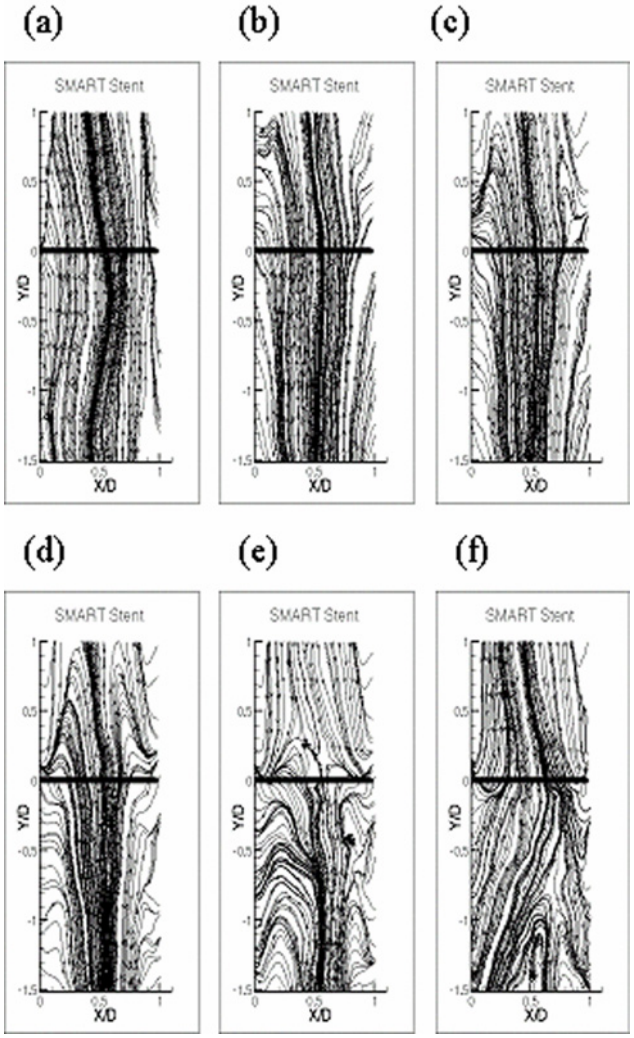

Figure 1.6: Flow development during phase 2 of the SMART stent as illustrated via streamlines. Flow is in the reverse part of the cycle (flow is from bottom to top). As flow begins to accelerates and begin the systolic part of the cycle, no vortical structures are observed. The time interval between each consecutive image is 0.005 seconds.

Phase 2 for the rigid cylinder stent can be observed in Fig. 1.7. A symmetric flow transition as seen in the SMART stent does not exist in the early stage of this phase. Moreover, two vortical structures can be found in our area of interrogation (Fig. 1.7d). The first vortical structure exists on the leading edge of the stent (Y/D =0 and X/D=0.8) and the top portion of the second vortex can be seen extending from X/D

= 0.5, Y/D = -1.3 to X/D = 0.5 to Y/D = 0.4 (Fig 1.7e). As forward flow progresses, the vortical structures diffuse into the mainstream of flow and the start of the next cycle begins (Fig. 1.7f).

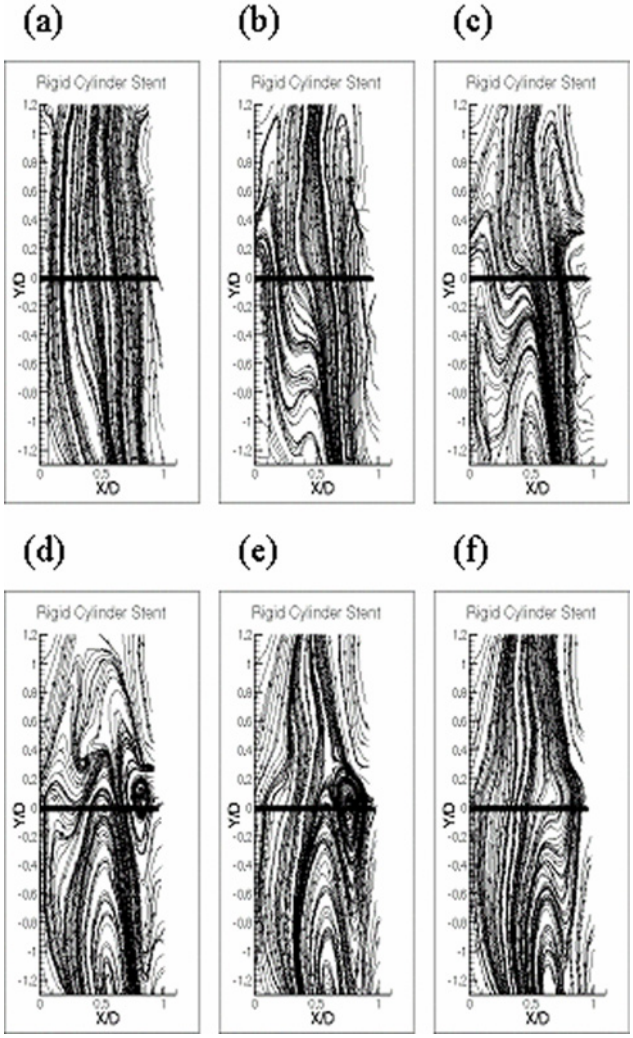

Figure 1.7: Flow development during phase 2 of the solid cylinder stent as illustrated via streamlines. Flow is in the reverse part of the cycle (flow is from bottom to top). As flow begins to accelerates and begin the systolic part of the cylcle, a vortical structure is observed on the leading edge of the stent. The time interval between each consecutive image is 0.005 seconds**.**

1.4. Discussion

We examined flow patterns in two types of stents in order to identify regions that promote non-laminar flow patterns that may diminish stent performance. Previous studies have shown that separated flow and vortical structures create high oscillating shear stress gradients, low shear stress, and abnormal physiological conditions that contribute to the development of intimal thickening and damage endothelial cells [9,10]. Therefore, we investigated the two phases that corresponded to the formation of vortical structures. This was accomplished by using a time-resolved DPIV system that enabled us to obtain a high spatial and temporal resolution of the flow during the pulse cycle. The results revealed that stent compliance largely dictates the level of flow disturbance. Specifically, the more compliant SMART stent experienced less flow disturbance and a smoother transition during flow reversal compared with the rigid cylinder stent.

During late systole/early diastole (phase 1) for both stent cases, we identified the formation of a shear layer that propagated upstream against the mean flow. The shear layer is associated with flow reversal due to a change of the pressure gradient in our vessel. Similar flow patterns are observed in a straight rigid pipe flow that is oscillated with a sinusoidal pressure gradient [20]. As flow decelerates during late systole, the upstream adverse pressure gradient acts upon the flow. Because the flow has the least kinetic energy on the boundary walls, flow first reverses at the boundary, creating the observed shear layer. Due to elasticity of the vessel, the oscillatory pressure propagates in a form of a wave and not an oscillatory bulk movement [21] concurring with the propagation of the shear layer observed in our experiment. In both stent cases, we observe that the shear layer begins to destabilize and roll into a vortex in the vicinity of the leading edge of the stent. During the late systole/early diastole (phase 1), the stent diameter is larger than the vessel diameter creating a cross-sectional area gradient at the leading edge of the stent. Due to this cross-sectional area decrease, the velocity gradient between the shear layer and mean flow increases, creating conditions that favor vortex formation.

As seen in phase 1 for both the SMART stent and rigid cylinder stent, the vortical formation generated from the shear layer develops into two counter rotating vortices

on the vessel walls (Fig. 1.4f and Fig. 1.5d). Since vortex kinematics do not allow vortex lines to be terminated on a solid wall or abruptly end in the middle of the flow, these vortex lines have to be connected. As a result it is concluded that for both cases, the two counter-rotating vortices formed a ring vortex. Figure 1.8 illustrates both the shape and the cross-section view of an axisymmetric ring vortex. Unlike Fig. 1.8, we did not observe a symmetric ring vortex. A small perturbation in the vortex strength distribution evoked a tilt of the vortex ring, triggering an interaction of the vortices with the walls that induced an asymmetric velocity. Placement of stents may factor into this initial tilt of the ring vortex. The induced asymmetric velocity forces the counter-rotating vortices to orbit each other in a motion superimposed with the mean flow, and inclines the ring vortex axis, as observed in Fig. 1.5d through Fig. 1.5h for the rigid cylinder stent. Figure 1.9 illustrates the sequence of events corresponding to this phenomenon. In Fig. 1.9a, two-counter rotating exists on the boundary of the walls. The mean flow is represented by three arrows pointing downwards. As these counter-rotating vortices apply a non-uniform force, they begin to rotate with respect to each other (Fig. 1.9b and Fig. 1.9c). As time progresses, the two counter-rotating vortices begin to diffuse away from the boundaries and diffuse into the flow (Fig. 1.9c and 1.9d). We note that although only one cycle of data is presented, flow behavior for both the SMART stent and rigid cylinder stent were repeatable for 4 cycles.

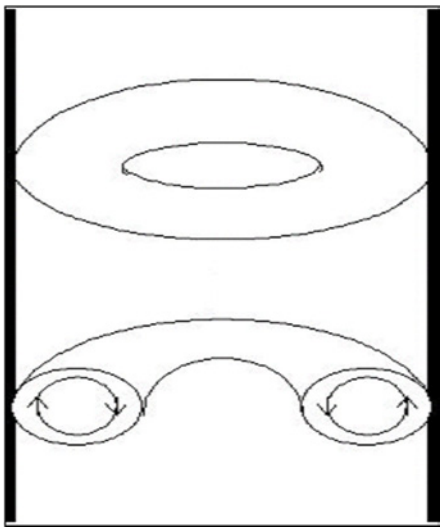

Figure 1.8: (Top): typical axisymmetric ring vortex is illustrated. (Bottom): the cross-section of an idealized ring vortex is shown, demonstrating the existence of two-counter rotating vortices. The thick black lines represent boundary walls.

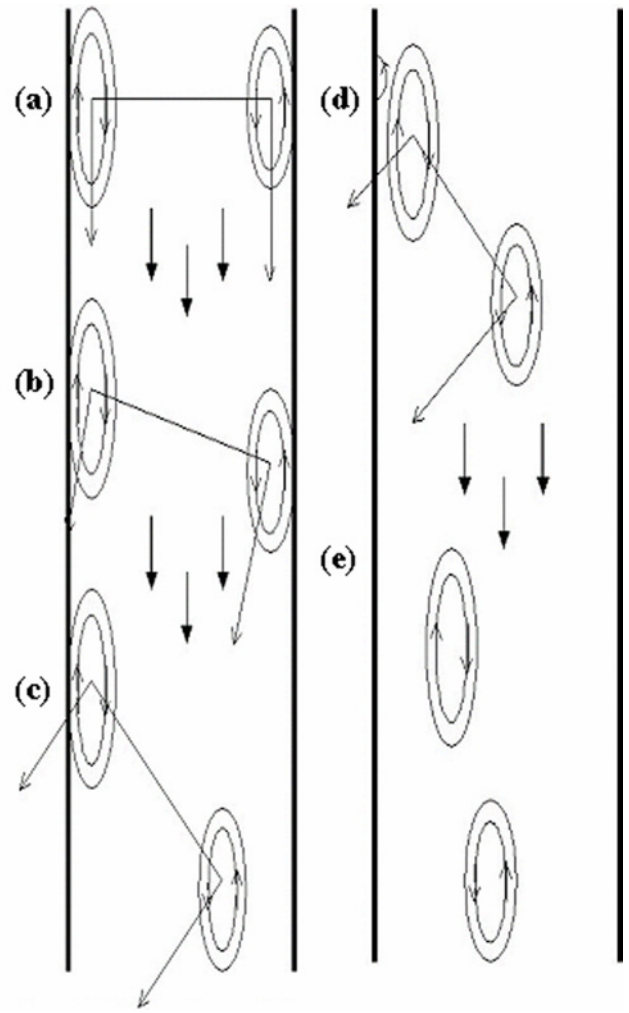

Figure 1.9: Illustration of vortex rotation superimposed with the free stream velocity.

The presence of the ring vortex may promote platelet attachment and alter normal physiologic shear stresses on endothelial cells. We observed that the ring vortex created for the rigid cylinder stent remains on the wall twice as long compared with the SMART stent and grew to 1.2 diameters in size (Fig. 1.4 and Fig. 1.5). This occurrence has a direct impact on the resident time of blood elements inside the stent. Also, as the ring vortex detached from the wall, the time for the ring vortex to diffuse into the flow for the rigid cylinder case was 50% longer compared to the case of the SMART stent, creating a longer disturbance inside the stent. Mechanical properties of stents (compliance mismatch) thus induce changes in the hemodynamic environment that may adversely influence the platelet behavior in the stents during early stages of

implantation, when acute thrombosis is known to occur. We note that since the ring vortex creates a 3-dimensional flow field, the location of the 2-dimensional plane of the cross-section view would affect the apparent size, but not the resident time of the ring vortex.

The ring vortex also induces separation of the boundary layer and the formation of secondary vortices on the wall. The transient boundary layer for our case was calculated to be 1.23 mm, which is in the order of 0.1 diameters and was determined by:

$$\delta_1 = \frac{r}{\alpha}$$

where r is the radius of the vessel and α is the Womersley parameter. These secondary vortices are not strong, and can be seen as a wave, which is a vortex, superimposed with the free stream in our flow field (Fig. 1.4d). In Fig. 1.10, an instantaneous zoomed image demonstrating secondary separation of the boundary layer is shown (T=0.571). Secondary vortices created in the boundary layer (within and adjacent to the stent) will vary the local shear stresses and consequently alter the shape of endothelial cells [22]. Moreover, since the resident time of the ring vortex for the rigid cylinder is greater compared with the SMART stent, the flow disturbances created by secondary separation will exist longer. We also note that due to the existence of a ring vortex and the interactions with secondary vortices, a 3-dimensional flow field exist that causes the flow to depart from the classical paradigm of axisymmetric Womersley flow.

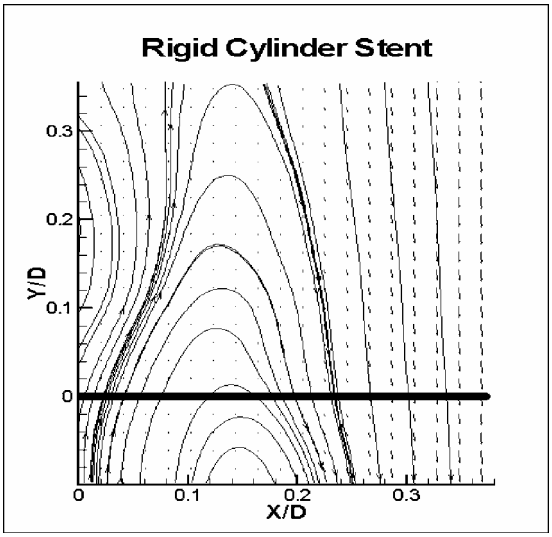

Figure 1.10: Secondary vortices in the transient boundary layer induced by the ring vortex in the solid cylinder case occurring at T=0.571.

In the late diastole/early systole (phase 2) part of the cycle, flow behaves with accordance to phase 1. Since the mean flow in phase 2 is in the opposite direction compared with phase 1, we anticipate the ring vortex to form in the distal edge of the stent. Although the distal edge of the stent is outside our area of interrogation, the streamlines seen in both the SMART stent (Fig. 1.6) and rigid cylinder stent (Fig. 1.7) indicate the formation of a ring vortex. Specifically, the top portion of the ring vortex for the SMART stent can be seen in Fig. 6e at Y/D = -1.0 to –1.5 and the top half of one of the vortices can be seen for the rigid cylinder stent in Fig. 6d at Y/D = -1, X/D = 0.5.

By comparing the late diastole/early systole phase of the two stents, we observe the formation of secondary vortices in the vicinity of the leading edge of the stent for the rigid cylinder stent (Fig. 1.7d). Similar to phase 1, the ring vortex in phase 2 for the rigid cylinder stent is more coherent (organized) creating a more disturbed flow compared with the SMART stent. These data indicate the adverse affect of compliance mismatch.

In the future, flow phenomena near stent struts and in the vicinity of the stents will be explored to examine the effects of different stent compliancy and geometry. The 3-D nature of the flow will also be examined.

Chapter 2

Effects of Womersley and Reynolds number on a Symmetric Compliant Bifurcation Model

2.1. Introduction

Cardiovascular disease is the number one killer in the United States for every year since 1900 except for 1918. Atherosclerosis represents one of the most severe cases of cardiovascular disease. It is widely accepted that pathogenesis of atherosclerosis is contributed from mechanical disturbances experienced by endothelial cells (ECs). ECs, which align the inner wall of vessels, are susceptible to fluid dynamic forces that can alter the cells normal function. Disturbed flow, which corresponds to flow separation and re-circulation region, has been shown to alter both ECs shape and orientation, particularly at regions of high wall shear stress gradient (WSSG), which are located at separation and reattachment points.

From clinical studies it is well known that atherosclerosis has preferred locations in the vascular system, primarily sited in the carotid arteries, coronary arteries, and in vessels supplying the lower extremities in the arterial system. In the vicinity of bifurcations, flow tends to separate forming re-circulation regions. In addition, due to the pulsatile character of blood flow during the deceleration part of the cycle, the flow becomes unstable and transition to turbulence may occur. The combination of the above-described phenomena generates abnormal wall shear stress (WSS) levels and high WSSG.

Flow in bifurcations has been studied both numerically and experimentally. The effects of pulsatility and bifurcation angle were investigated by Jou and Berger [23] and Nazemi et al. [24]; however the later also examined the effects of stenosis. Zhao et al. [25] measured velocity fields and wall shear stress. Rindt and Steenhoven [26] observed the effects of changing the sinus angle, the angle between the main branch and the carotid sinus. Lorthois et al. [27] used numerical simulations to quantify the shear stresses. They showed that the risk of embolus might be greater for moderate stenosis than severe ones. Although understanding of the flow in bifurcations was

significantly enhanced by these studies, all the investigations mentioned above- were limited by the use of rigid models, which alleviates some of the complexity of the problem. Recent experimental techniques have been utilized in analyzing fluid dynamics through bifurcations. Perktold et al. [28] used Laser-Doppler Velocimetry (LDV) to compare and validate his numerical solutions of flow through a rigid coronary bifurcation model using unsteady flow. Gijsen et al. [29] obtained data via Laser-Doppler Anemometry (LDA) to compare non-Newtonian and Newtonian fluid in a rigid bifurcation using steady flow. For the non-Newtonian fluid the axial velocity profile was flattened, had lower velocity gradients at the divider wall, and higher velocity gradients at the non-divider wall. No flow separation, was observed for the Newtonian fluids. Carr and Kortha [30] used flow visualization techniques to look at the shape of a separation surfaces for Reynolds number ranging from 10 to 200 for a 90 degrees and a 45 degrees bifurcation angle in a rigid model. At low Reynolds numbers the separation surfaces are curved in a convex manner, bulging away from the opening of the side branch. Increasing the Reynolds number causes the surface to become concave. The branching angle was found not to have any noticeable effect on the separation surface shape. Lee and Tarbell [31] used flow visualization to observe how vessel compliance and the phase angle between pressure and flow waves (impedance phase angle) affect wall shear rate distribution for both rigid and non-rigid models under unsteady flow conditions. This study indicates that in the low shear rate zone, the unsteadiness of the flow greatly reduces the mean (time-averaged) wall shear rate level. Vessel wall motion reduces the wall shear rate amplitude (time-varying component) up to 46 percent depending on the location and phase angle in the model. These findings manifest the need for employing compliant (non-rigid) models. Palmen et al. [32] used hydrogen-bubble flow visualization to capture how the Reynolds and Wormersley numbers affect the flow characteristics, and the mass flow rate ratio in a rigid bifurcation (carotid) with mild stenosis.

The majority of the previous experimental studies employ either flow visualization techniques or LDV/LDA. Flow visualization is a great tool to better understand the flow characteristics in a bifurcation, resulting into a global view of the flow. However, only qualitative information can be obtained. LDV/LDA provides quantitative measurements of two or three velocity components at different locations

in the bifurcation. But a great limitation rises from the inability of the method to generate a global view of unsteady flow fields, since velocities are measured at a single point every time. Therefore, tedious and careful traversing of the measurement volume is required in order to reconstruct the entire flow field. This procedure becomes much more difficult for unsteady/pulsatile flow fields, where one should insure that the phenomenon is periodic repeatable and accurate timing is feasible in order to phase-trigger the data acquisition process. Thus a global description of the flow via LDV can only be reconstructed in a statistical manner and significant details of the instantaneous characteristics of the flow are suppressed.

In the present study, we use time-resolve Digital Particle Image Velocimetry (DPIV) to explore the fluid dynamics phenomena in a symmetric compliant bifurcation. We studied the effects of the Womersley and the Reynolds numbers under pulsatile flow conditions. New insight of the fluid mechanics is revealed. The flow topology results indicate that the formation of coherent vortices in the vicinity of the bifurcation apex is governed by physical process that dictates the energy and strength of the formed vortices. This is manifested by the identification of a characteristic dimensionless time-scale that combines the impulsive vortex formation with the inertia of the unsteady flow.

2.2. Methods

2.2.1. Experimental Setup

The experimental setup was comprised of a computer controlled gear pump (Ismatec Inc., Glattburgg, Switzerland, drive 'MV-Z' with micropump pumphead model 201) connected to a compliant bifurcation model, 8 inches in length. The bifurcation model was contained in an acrylic box submerged in a bath with the same fluid as the working fluid in order to allow for optical access and account for index of refraction induced distortions. A flexible container was introduced before the test section to act as a low pass filter eliminating high frequency fluctuations generated by the pump. Two intravascular pressure transducers (Millar Instruments, Inc. Houston, TX, model no. SPC-330A) were inserted proximal and distal to the bifurcation model recording the instantaneous pressure. Upstream and downstream flow rates were measured with two ultrasonic flow meters (Transonic Systems Inc., Ithaca, NY, Model

T110) with a 30 Hz frequency response. An 8-channel, 16-bit, 1MHz data acquisition board was used for the digital to analog conversion and data recording. A schematic representation of the experimental setup is presented in Fig. 2.1.

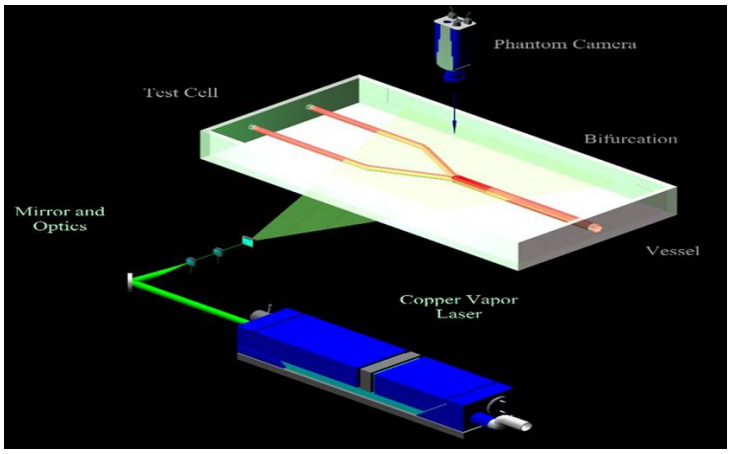

Figue 2.1: Experimental Setup.

2.2.2. Bifurcation Geometry

The bifurcation model was fabricated with silicone Fig. 2.2. The bifurcation diameters were scaled approximately 300% compared to the carotid arteries to better resolve the flow and attain high accurate measurements near the boundaries. The bifurcation model was one inch in the mother tube and 0.75 inch in the daughter tubes with 2 mm thickness. The bifurcation angle was 50 degrees between the two daughter tubes.

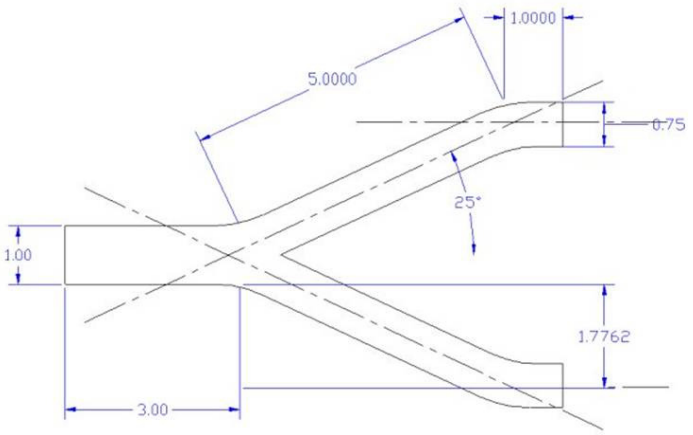

Figure 2.2: Bifurcation geometry of silicone model.

2.2.3. Flow Waveform

To isolate the effects of Womersley number and Reynolds number at the bifurcation, the mean Reynolds number was varied from 80 to 440 with Womersley number of 8.5 (110 beats/min) and 10.5 (166 beats/min). Table 2.1 summarizes the six cases. The flow conditions generated corresponded to in vivo exercise conditions. A sinusoidal wave form with a 30% duty cycle was inputted. Flow rate for all six cases are shown in Figure 2.3. The pressure range was in the physiological range of 70-110 mmHg.

Table 2.1: Parameter definition for each case.

Case	
1	Re # 80, W # 8.5
2	Re # 280, W # 8.5
3	Re # 440, W # 8.5
4	Re # 80, W # 10.5
5	Re # 280, W # 10.5
6	Re # 440, W # 10.5

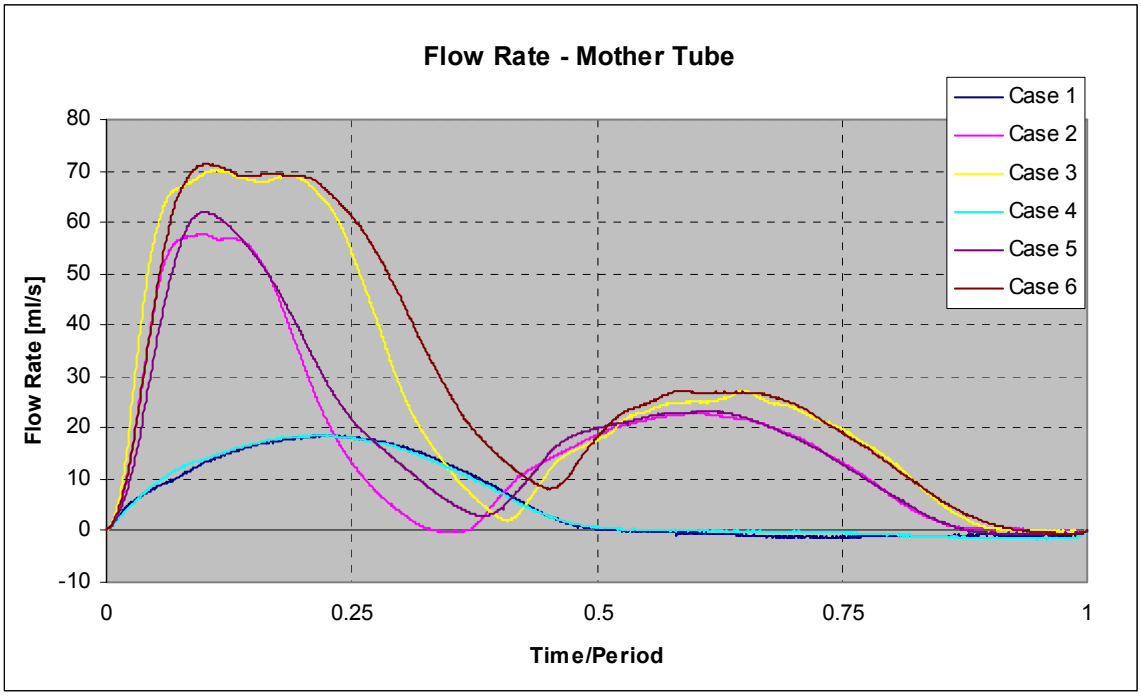

Figure 2.3: Flow rate measurements for each case within the mother tube.

2.2.4. DPIV System

A pulsing laser beam (55Watts) was guided through a series of mirrors and lenses in order to form a 2 mm thick laser sheet that illuminated the planar area of interrogation. Neutrally buoyant fluorescent particles were used as flow tracers in the working fluid (a glycerin/water mixture). The particle diameter was approximately 30 microns to insure that they accurately followed the path of the flow with limited response lag to turbulent fluctuations. A fast CMOS digital camera (500 frames/sec) was used to record the instantaneous positions of the particles. The recorded images were processed in order to evaluate the instantaneous velocity fields by applying a dual frame dynamically adaptive multigrid cross-correlation scheme. The accuracy of the method was show to be independent of velocity gradients and the rotationally of the flow and delivers superior spatial resolution. For the conditions of the present experiments the accuracy was estimate to be in the order of 0.05 pixels with a velocity vector grid spacing of 540 microns. The camera and D/A board were synchronized resulting in simultaneous pressure, flow rate measurements and DPIV data.

2.3. Basic Concepts

2.3.1. Flow Separation

In bifurcation geometries, an adverse pressure gradient always exists due to an increase in the cross-sectional area of the apex compared with the inlet. Due to the high inertia of the flow during high systole, the adverse pressure gradient has minimal effects on the fluid dynamics within the apex region. During the late systolic phase of the cycle the adverse pressure gradient begins to decelerate fluid elements near the boundary. As the bulk flow velocity continues to decrease, the adverse pressure gradient induces a separation region within the apex region. For low Reynolds number, the separation region begins to spiral into a coherent vortex as seen in Fig. 2.4a. For high Reynolds numbers, the vortex is observed as a wave, resulting from the superposition of the vortex with the free stream (Fig. 2.4b).

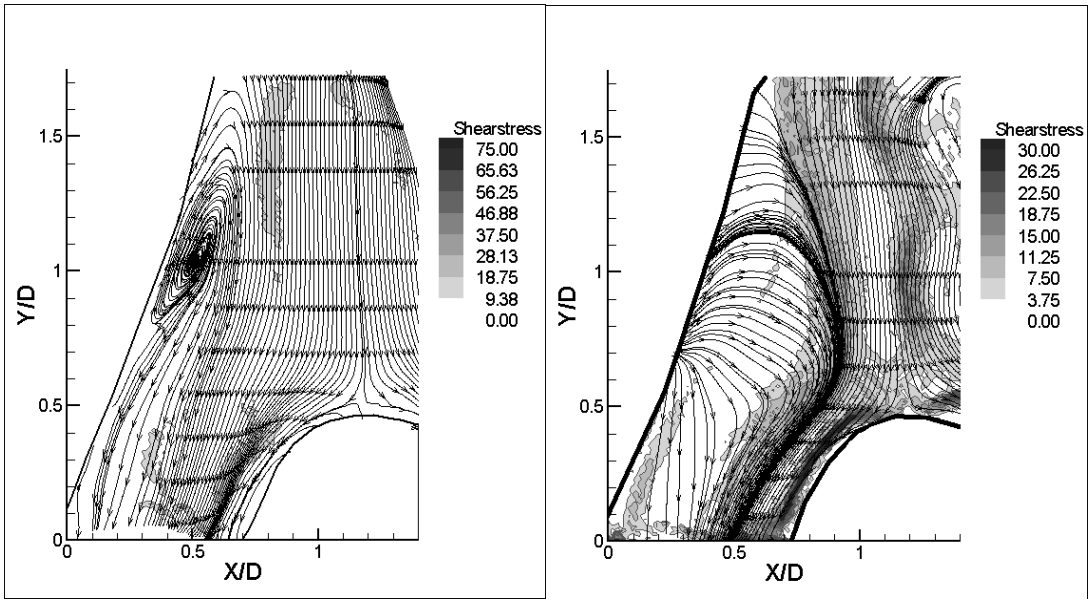

Figure 2.4: A) Instantaneous image of a coherent vortex occurring during the deceleration part of the cycle (left side). B) Instantaneous image of a vortex seen as a wave (right side).

As flow separates, more phenomena are observed. Vorticity generated on the vessel walls begins to detach and migrate into the flow. We note that in the data presented herein, we have superimposed the flow streamtraces with a non-dimensional shear stress contour plot, which provides similar information as vorticity. Fig. 2.5a, illustrates an instantaneous image of our flow field where high shear exists on the

boundary walls. As flow separates, the high shear stress values detach from the wall and diffuse into the main flow (Fig. 2.5b). Deceleration and recirculation regions of the fluid elements near the bifurcation apex and the detachment of the shear layer, reveal the onset of separation.

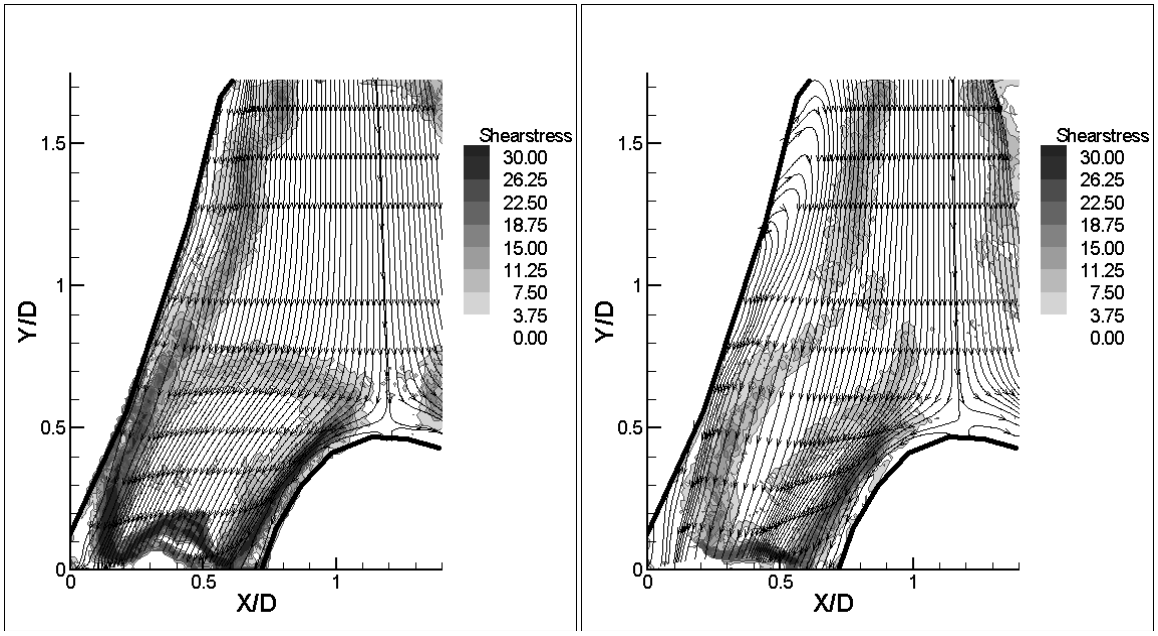

Figure 2.5: A) Instantaneous image illustrating high shear stress located on the boundary walls (left side). B) Instantaneous image illustrating the migration of high shear stress into the main flow as separation occurs (right side).

2.3.2. Characterization of vortex

The vortex size and strength is related to how much vorticity a vortex can endow. The characteristic size of the vortex will be dictated by the diameter of the vessel. Since our flow is bounded, the vorticity fed to the vortex is generated on the boundary walls. Under pulsatile flow conditions the vorticity generation on the wall is maximum during the systolic part of the cycle while the rate of vorticity flux is proportional to the temporal variation of the pressure gradient. Subsequennly the vortex development can be described by three scenarios. As the flow decelerates during diastoly is reduced and eventually instantaneously stops. The first scenario will predict that vorticity supplying the vortex ends before the maximum strength is reached. Second, the vortex reaches its full potential as vorticity being generated is ceased. Lastly, the vortex reaches its full capacity before the completion of the systoly therfore the vorticity flux from the wall

into the flow continues. As a result the vortex saturates and the excess vorticity generated forms into smaller-scale vortices, indicating the occurrence of pinch-off. The formation of additional vortices in the flow enables us to identify when saturation occurs and can be shown in our flow field by the existence of saddle points. Saddle points occur when two or more vortices develop in the flow and is represented in Fig. 2.6a. Flow topology teaches us that the presence of two vortices in the flows represented by nodes will be accompanied by the presence of one saddle point. Figure 2.6b illustrates an example of a saddle point in our data.

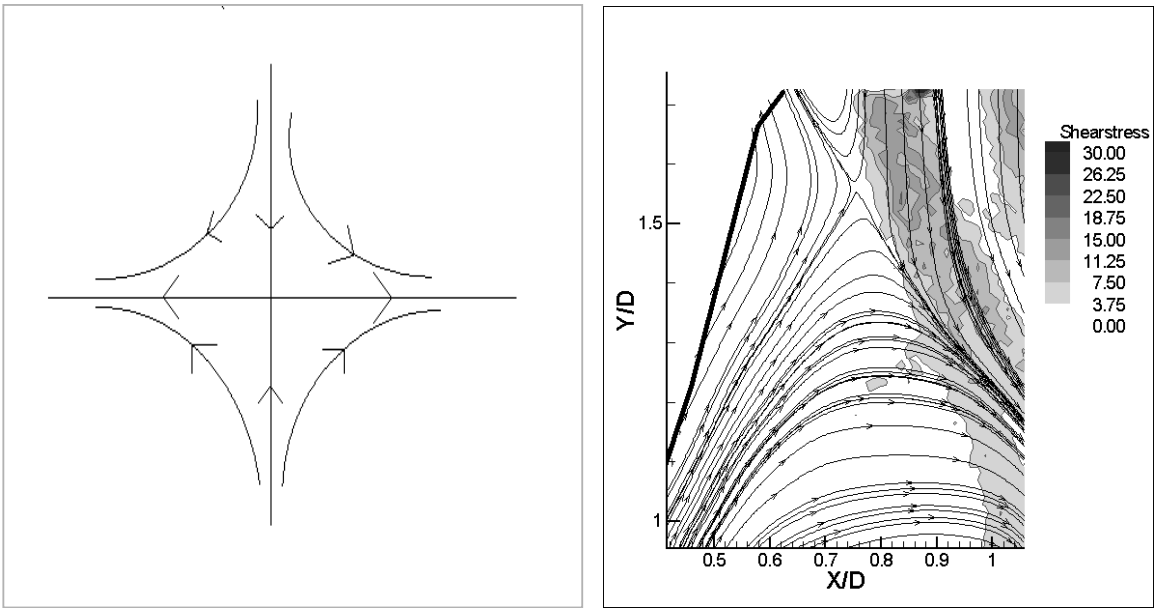

Figure 2.6: A) Illustration of a saddle point (left side). B) An instantaneous image of our flow field demonstrating the occurrence of a saddle point (right side).

2.3.3. Governing parameters of vortex formation

Similar to Gharib et al. [33], we want to calculate the 'vortex formation number' that will identify when the vortex in our bifurcation geometry is endowed with the maximum amount of vorticity. In Gharib et al. model, a piston/cylinder arrangement was used to generate a ring vortex in an unbounded flow. They showed that the dimensionless parameter governing the ring vortex formation is a number the stroke ratio (L/D). The stroke ratio value in their experiment corresponded to the length (L) of the column of fluid being pushed by the piston versus the diameter (D) of the

orifice. They also illustrated that the stroke ratio (L/D) is equivalent to the non-dimensional value of $U_p t/D$, where t is the instantaneous time, D is the diameter of the orifice, and U_p represent the running mean of the piston velocity and is described by

$$U_p = 1/t \int_0^t u_p dt .$$

This formulation if most appropriate for pulsatile flow conditions since there is no mechanical piston driving te flow however the running mean of the velocity can be determined by the flow rate. In calculating the vortex formation number for our bifurcation geometry, we used a non-dimensional value of ($U_m t/D$), where t was the instantaneous time instant, D was the diameter of the inlet tube, and U_m represents the running max velocity of the inlet tube and is calculated by $U_m = 1/t \int_0^t u_m dt$. The maximum velocity values U_m, was obtained by our DPIV results. The value of U_m was then divided by the instantaneous Reynolds number. The Reynolds number, Re was defined as $\mathrm{Re} = \frac{D * u_m}{\nu}$, where D was the diameter of the inlet vessel, u_m was the maximum velocity of the inlet tube, and ν was the kinematic viscosity of the flow.

2.4. Results

Figure 2.7 illustrates flow conditions for case 1 during which flow separation occurs. The mean Reynolds number for case 1 was 80, the peak Reynolds number was 320, with a Womersley parameter of 8.5. These images correspond to a t* interval of 0.39 to 0.51 (late systole), where flow is decelerating and the adverse pressure gradient induces separation on the outer vessel of the bifurcation. Figure 1b illustrates the first stage of the separation region where the shear stress deviates away from the boundary walls. In Figure 1c, the separation region evolves into a coherent vortex with the center position at approximately X/D = 0.6, Y/D =1.1. The migration of the vortex towards the center of the bifurcation and reversal of flow on the boundary is shown in Figure 1c. Since no secondary vortices appear to exist, we assume that pinch-off never occurs, and the vorticity generated is ceased before the instant flow is reversing on the boundary. This instant occurs at 0.488 t* (Fig. 2.8), which has a corresponding L/D

value of 0.772 and an instantaneous Reynolds number of 134 resulting in the vortex formation number value of 0.0057.

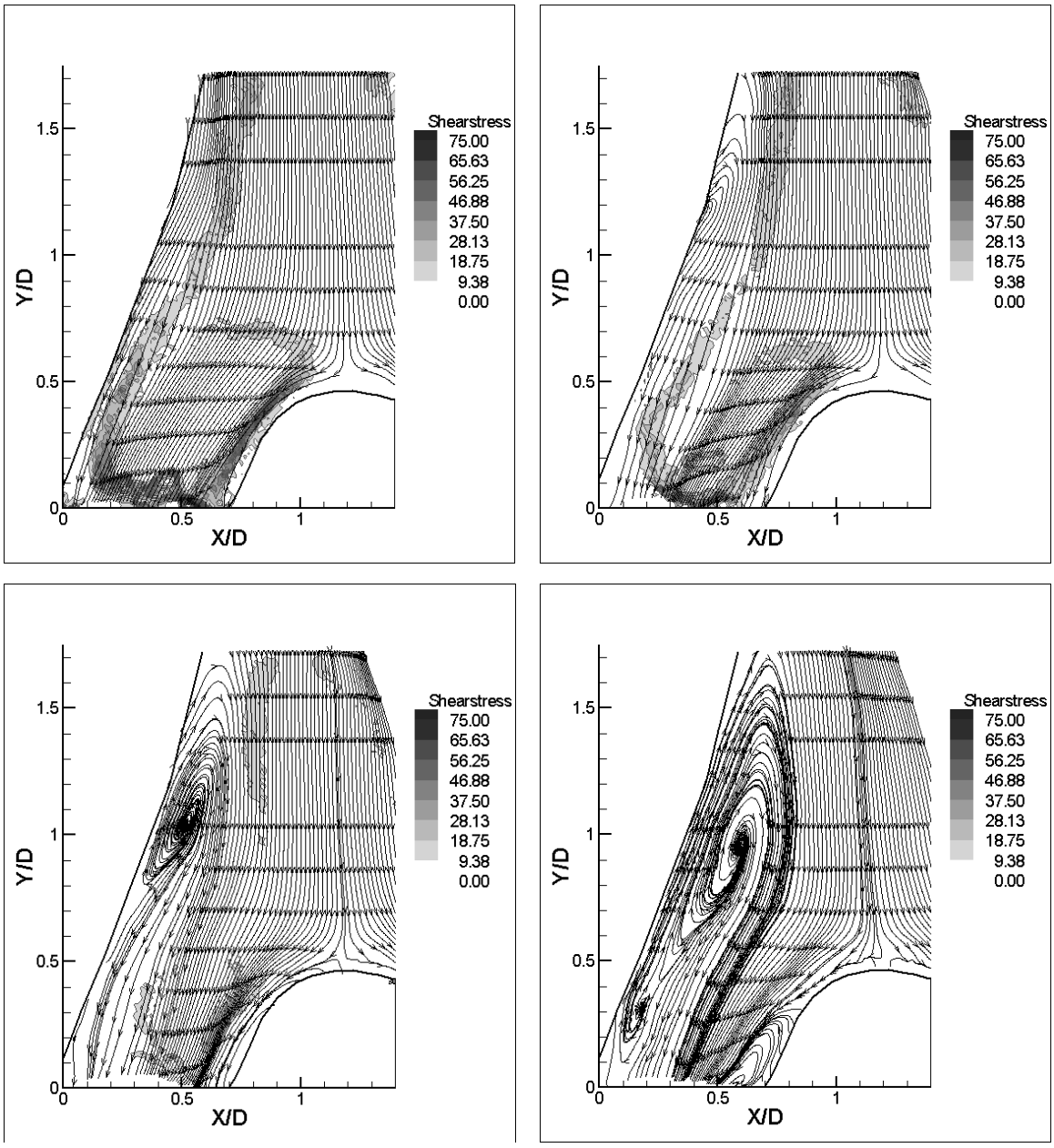

Figure 2.7: Instantaneous flow images illustrating flow conditions during declaration phase of the cycle for case 1. (a) Flow is beginning to decelerate (top left). (b) Flow begins to decelerate more and roll into a spiral (top right). (c) Flow transitions into a clock-wise vortex (bottom left). (d) Flow remains in spiral motion and begins to grow larger (bottom right).

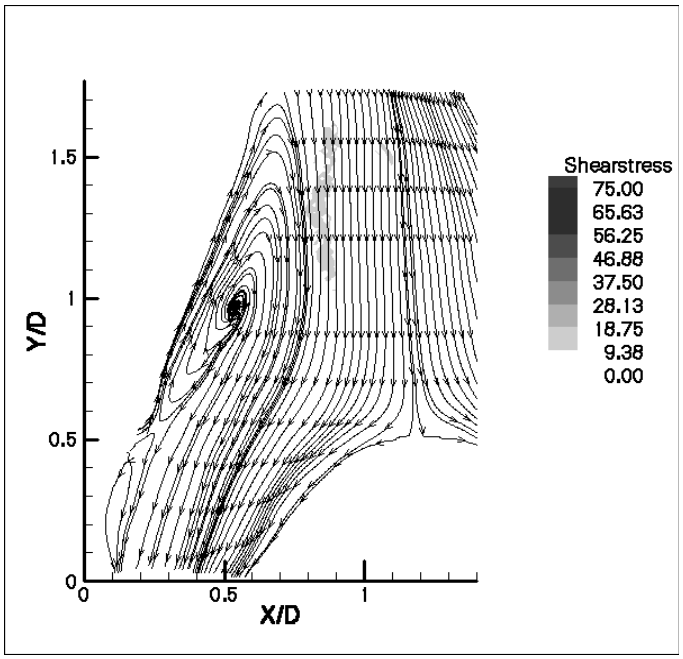

Figure 2.8: Instantaneous flow image illustrating flow field before flow begins to reverse on the boundary and thus ceasing the production of vorticity.

In Fig. 2.9, flow behavior for case 2 during the late systole is presented. The mean Reynolds for this case was 280, the peak Reynold number was 790, with a Womersley parameter of 8.5. The images correspond to the t* interval of 0.32 to 0.54. Figure 2.9a and 2.9b, illustrates the start and the expansion of the separation region. In figure 2.9c, the separation region is shown to evolve into a clockwise vortex with its center position at X/D = 0.7, Y/D = 0.55. A second separation region is also observed in this instance, confirming that the vortex has accumulated the maximum vorticity from the vessel wall and pinch-off has occurred. As time continues, the second separation region is shown to have rolled into a small vortex with its center position at X/D = 0.6, Y/D = 1.3 (figure 2d). The instant that pinch-off occurs was calculated to be at a t* value of 0.404 and is seen in figure 2.10. In this figure, a saddle point can be identified at X/D = 0.7, Y/D =1.7 indicating the existence of a second vortex. At this moment, the vortex formation number was 0.0106 which corresponded to a L/D value was 5.51 and the instantaneous Reynolds number was 519.

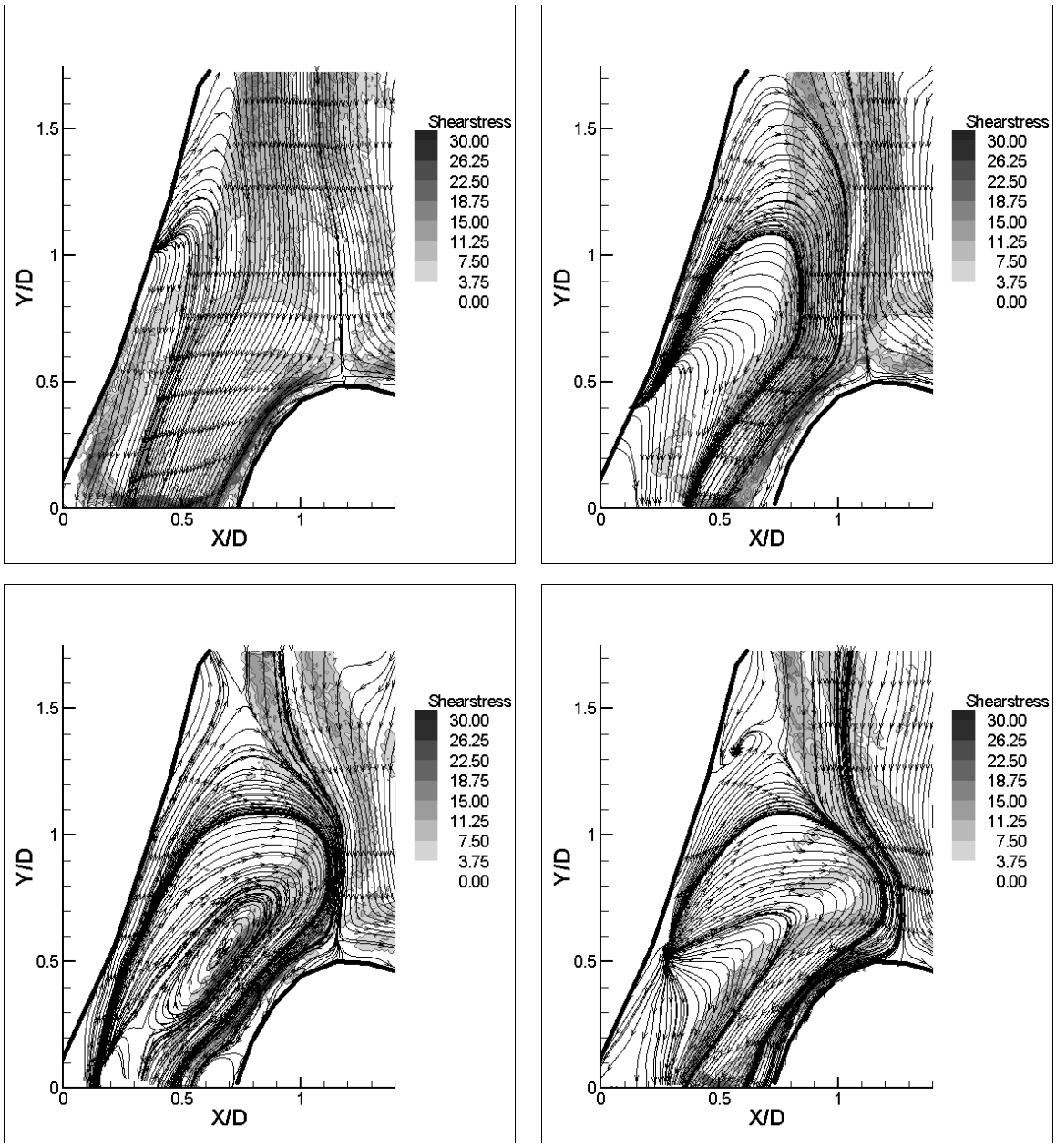

Figure 2.9: Instantaneous flow images illustrating flow conditions during declaration phase of the cycle for case 2. (a) Flow is beginning to decelerate (top left). (b) Flow begins to decelerate more and roll into a spiral (top right). (c) Second separation begins to roll into a spiral motion confirming the occurrence of pinch-off (bottom left). (d) Second separation region is shown to have rolled into a small vortex with its center position at X/D = 0.6, Y/D = 1.3 (bottom right).

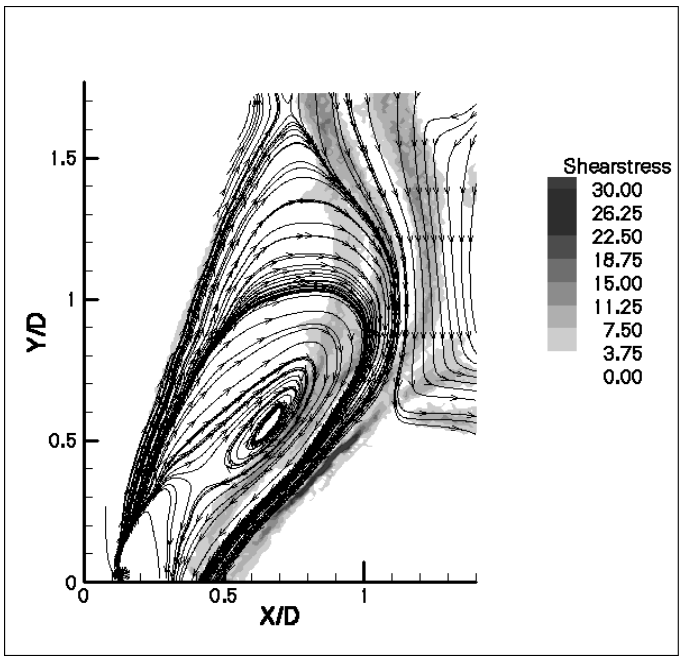

Figure 2.10: Instantaneous flow image illustrating the occurrence of a saddle point and thus ceasing the production of vorticity.

Flow behavior during late systole for case 3 is shown in Fig. 2.11. The mean Reynolds number for case 3 was 380, the peak Reynold number was 1610, and the Womersley parameter was 8.5. The images in Fig. 2.11 correspond to a t* interval of 0.35 to 0.47. In Fig. 2.11a, flow is separated. In Fig. 2.11b, a second separation is seen to occur at X/D = 0.6, Y/D = 1.7. As in case 2, a second separation region confirms that saturation has occurred and that the vortex has reached levels of maximum vorticity. Figure 2.11c, shows that the second separation region has evolved to a small coherent vortex. This vortex is seen to migrate downstream, adjacent to the boundary, in Fig. 2.11d. The instant of pinch-off was determined to be at a t* value of 0.378 and is shown in Fig. 2.12 where the corresponding L/D value was 8.34 and the instantaneous Reynolds number was 851. From these values, the vortex formation number was calculated to be 0.0098.

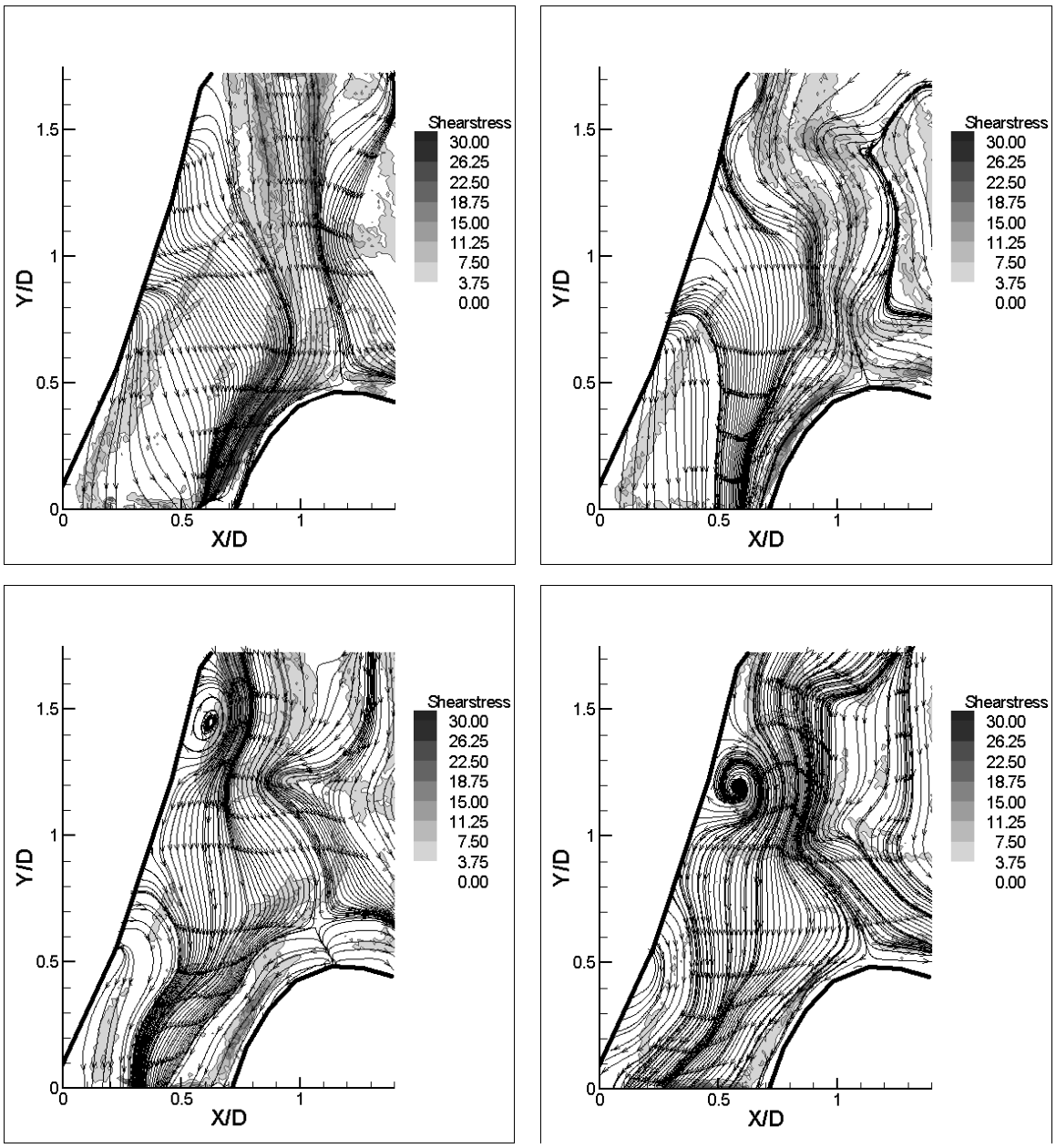

Figure 2.11: Instantaneous flow images illustrating flow conditions during declaration phase of the cycle for case3. (a) Flow is beginning to decelerate (top left). (b) Flow begins to decelerate more and form a separation region (top right). (c) Second separation begins to roll into a spiral motion confirming the occurrence of pinch-off (bottom left). (d) Second separation region is shown to have rolled into a small vortex with its center position at X/D = 0.6, Y/D = 1.2 (bottom right).

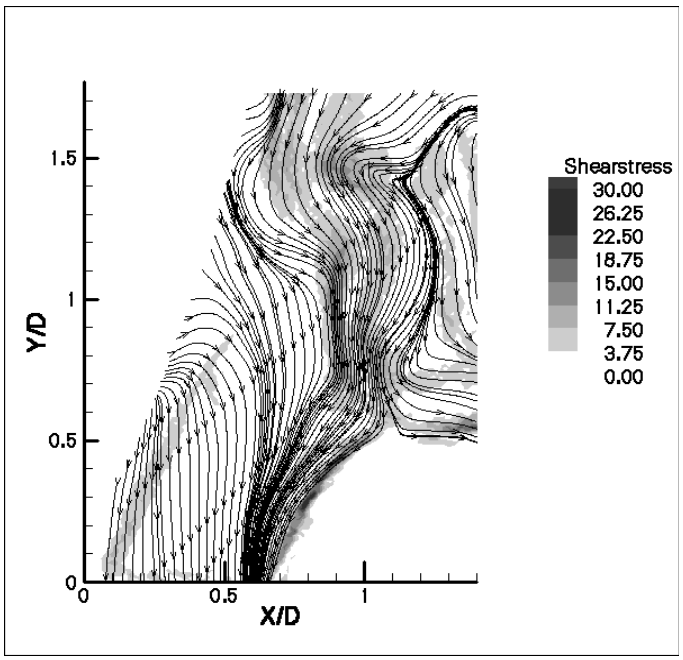

Figure 2.12: Instantaneous flow image illustrating the instant a second vortex is observed, thus ceasing the production of vorticity.

Figure 2.13 shows the flow characteristic during the late systolic part of the cycle for case 4. The mean Reynolds number for this case was 80, peak Reynolds number was 225, and the Womersley parameter was 10.5. The images in Fig. 2.13 correspond to a t* interval of 0.39 to 0.57. In Fig. 2.13a, flow is observed to separate as indicated by deviation of the shear stress contour plots from the bifurcation boundary. Separation further evolves in Fig. 2.13b and as time continues, it is rolled into a vortex with its center position at X/D = 0.5, Y/D = 1.0 (Fig. 2.13c). The location of this vortex is very similar to the observed vortex in case 1, which also has a mean Reynolds number of 80 but with a lower Womersley parameter of 8.5. Since no additional vortices are apparent in the flow, we assume that the vorticity generated on the flow is ceased when flow reversal occurs on the boundary walls. This instant occurs at a t* value of 0.541 and is illustrated in Fig. 2.14. At this instant, the vortex formation number was determined to be 0.0087, which corresponded to a L/D value of 1.46 and an instantaneous Reynolds number value of 168

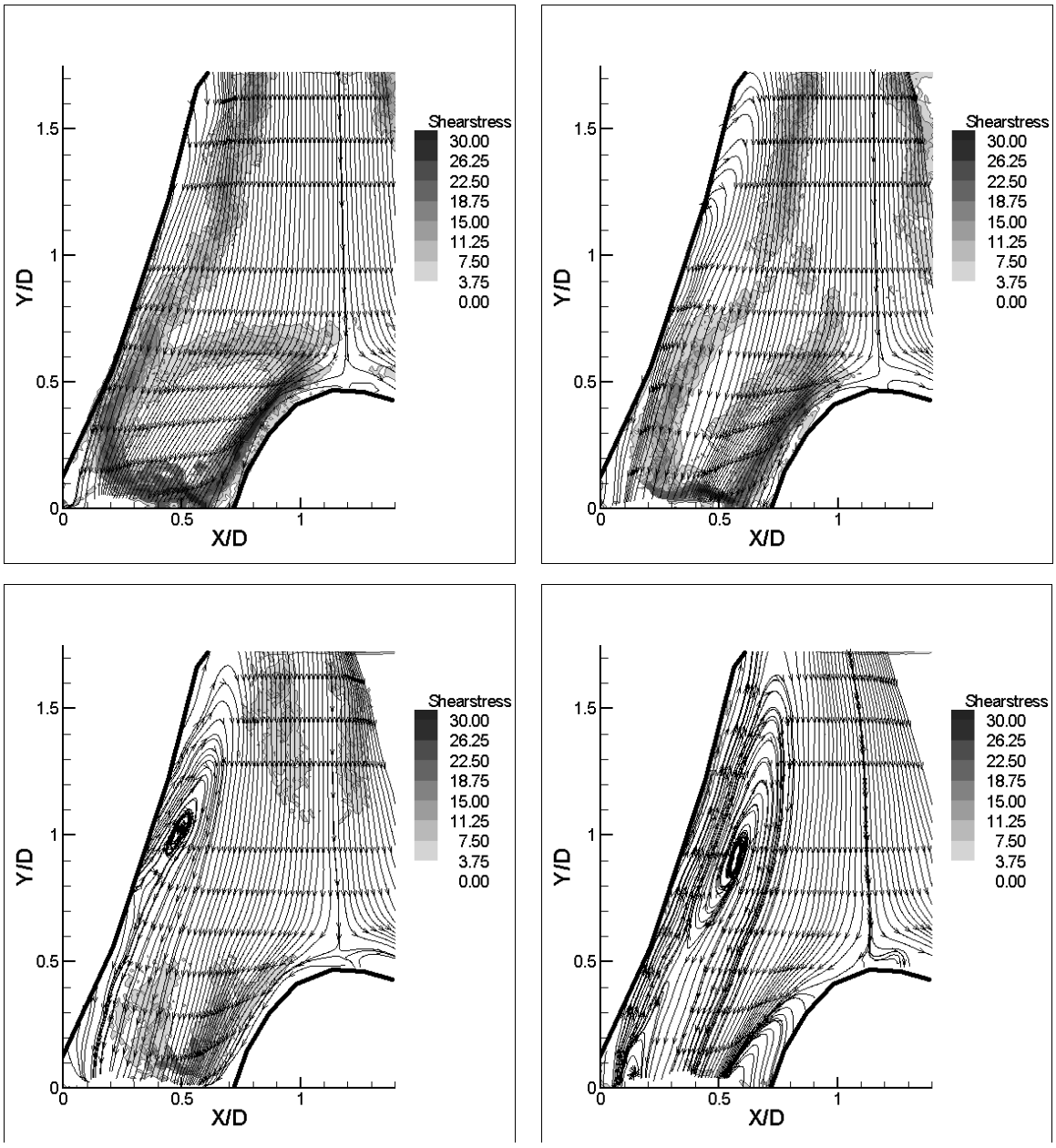

Figure 2.13: Instantaneous flow images illustrating flow conditions during declaration phase of the cycle for case4. (a) Flow is beginning to decelerate (top left). (b) Flow begins to decelerate more and roll into a spiral (top right). (c) Flow transitions into a clock-wise vortex (bottom left). (d) Flow remains in spiral motion and begins to grow larger (bottom right).

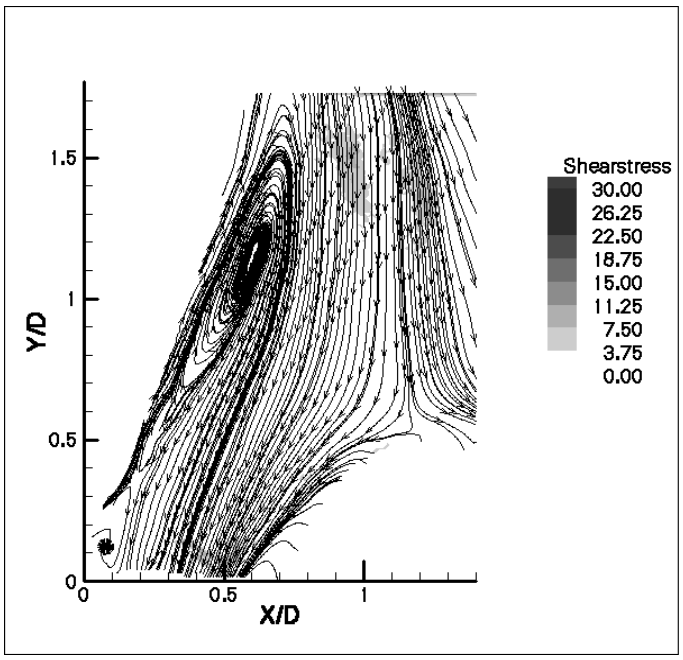

Figure 2.14: Instantaneous flow image illustrating flow field before flow begins to reverse on the boundary and thus ceasing the production of vorticity.

In Fig. 2.15, flow behavior during late systole for case 5 is illustrated. The mean Reynolds for this case was 280, the peak Reynolds number was 775, and the Womersley parameter was 10.5. The images correspond to a t* interval of 0.50 to 0.68. Figure 2.15a and 2.15b illustrate the separation region evolving to a clockwise vortex. In Fig. 2.15d, a second clockwise vortical structure is clearly visible with its center position at X/D = 0.6, Y/D = 1.45. The instant where the formation of the second vortex is visible in our area of interrogation occurs at t* of 0.587 and is demonstrated in Fig. 2.16. At this instant the value of L/D was calculated to be 5.13 and the instantaneous Reynolds number was 510, which corresponded to a vortex formation number of 0.0101.

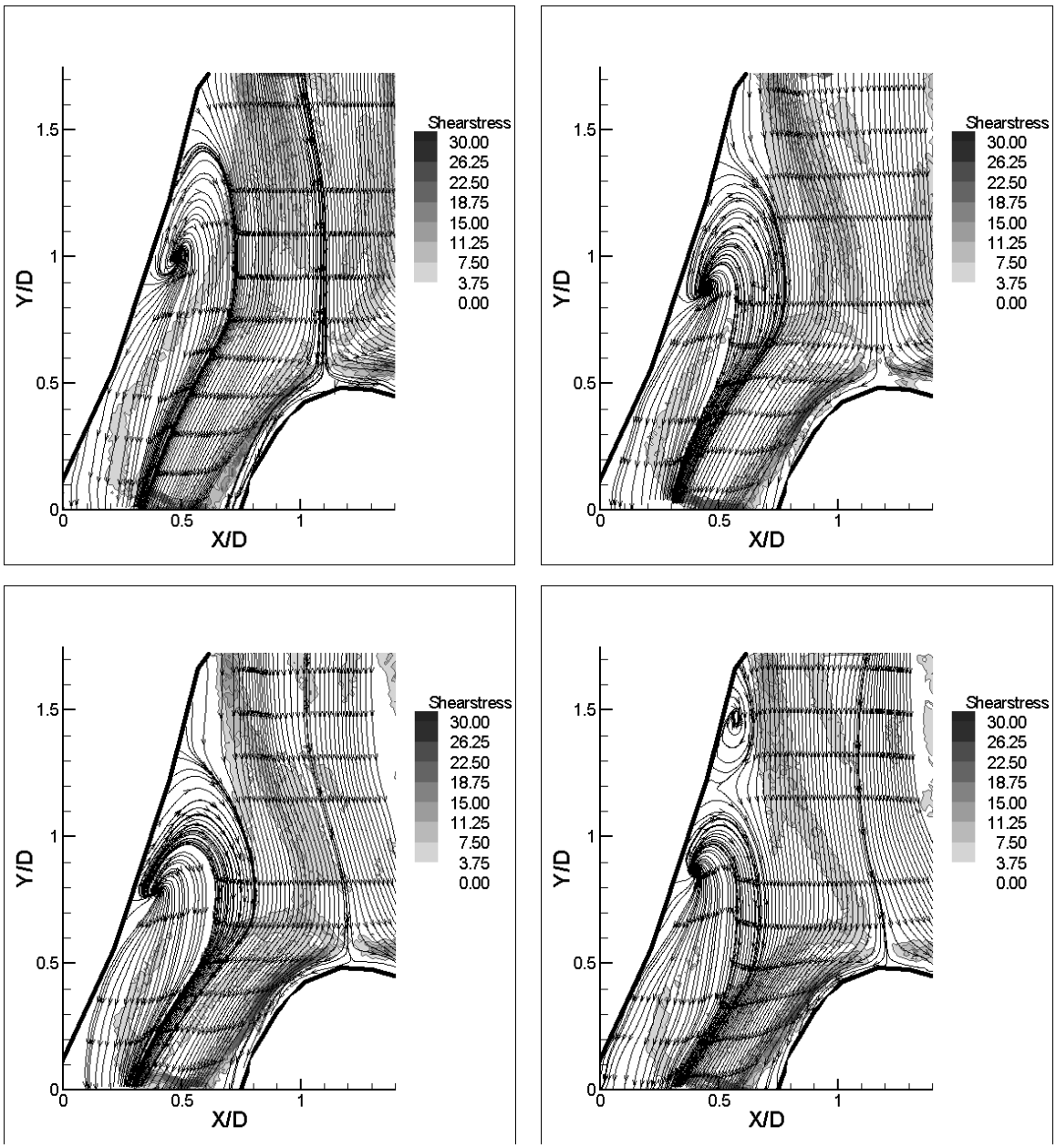

Figure 2.15: Instantaneous flow images illustrating flow conditions during declaration phase of the cycle for case 5. (a) Flow is beginning to decelerate (top left). (b) Flow begins to decelerate more and roll into a spiral (top right). (c) Second separation begins to roll into a spiral motion confirming the occurrence of pinch-off (bottom left). (d) Second separation region is shown to have rolled into a small vortex with its center position at X/D = 0.5, Y/D = 1.5 (bottom right).

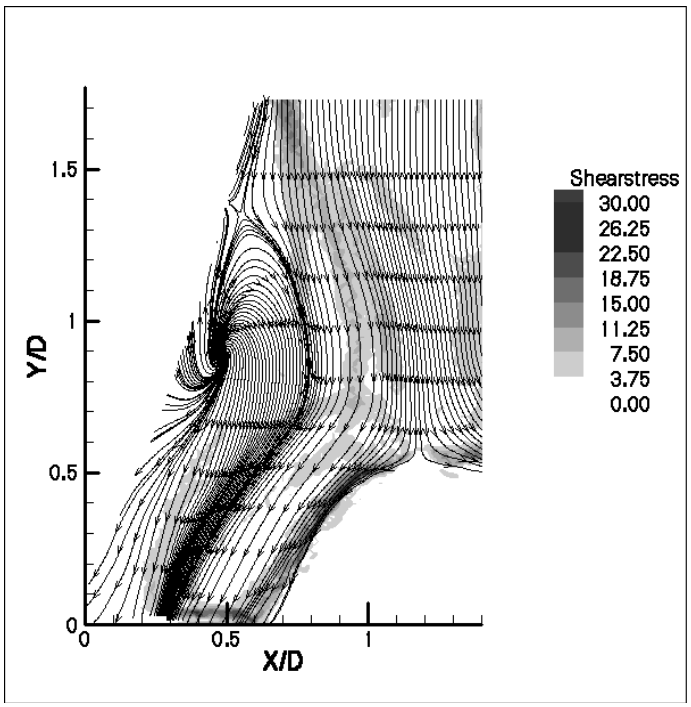

Figure 2.16: Instantaneous flow image illustrating the occurrence of a saddle point and thus ceasing the production of vorticity.

Flow behavior during late systole for case 6 is shown in Fig. 2.17. The mean Reynolds number for case 6 was 380, the peak Reynolds number was 1240, and the Womersley parameter was 10.5. The images in Fig. 2.17 correspond to a t* interval of 0.46 to 0.64. In Fig. 2.17a, flow is separated. In Fig. 2.17b, a second separation is seen to occur at X/D = 0.6, Y/D = 1.4. This second separation indicates that pinch-off has occurred. The instant where the second separation was identified at a t* value of 0.581 and is seen in Fig. 2.18. At this specific time, the vortex formation number was determined to be 0.0095, which corresponded to an L/D value of 7.68 and an instantaneous Reynolds number of 805.

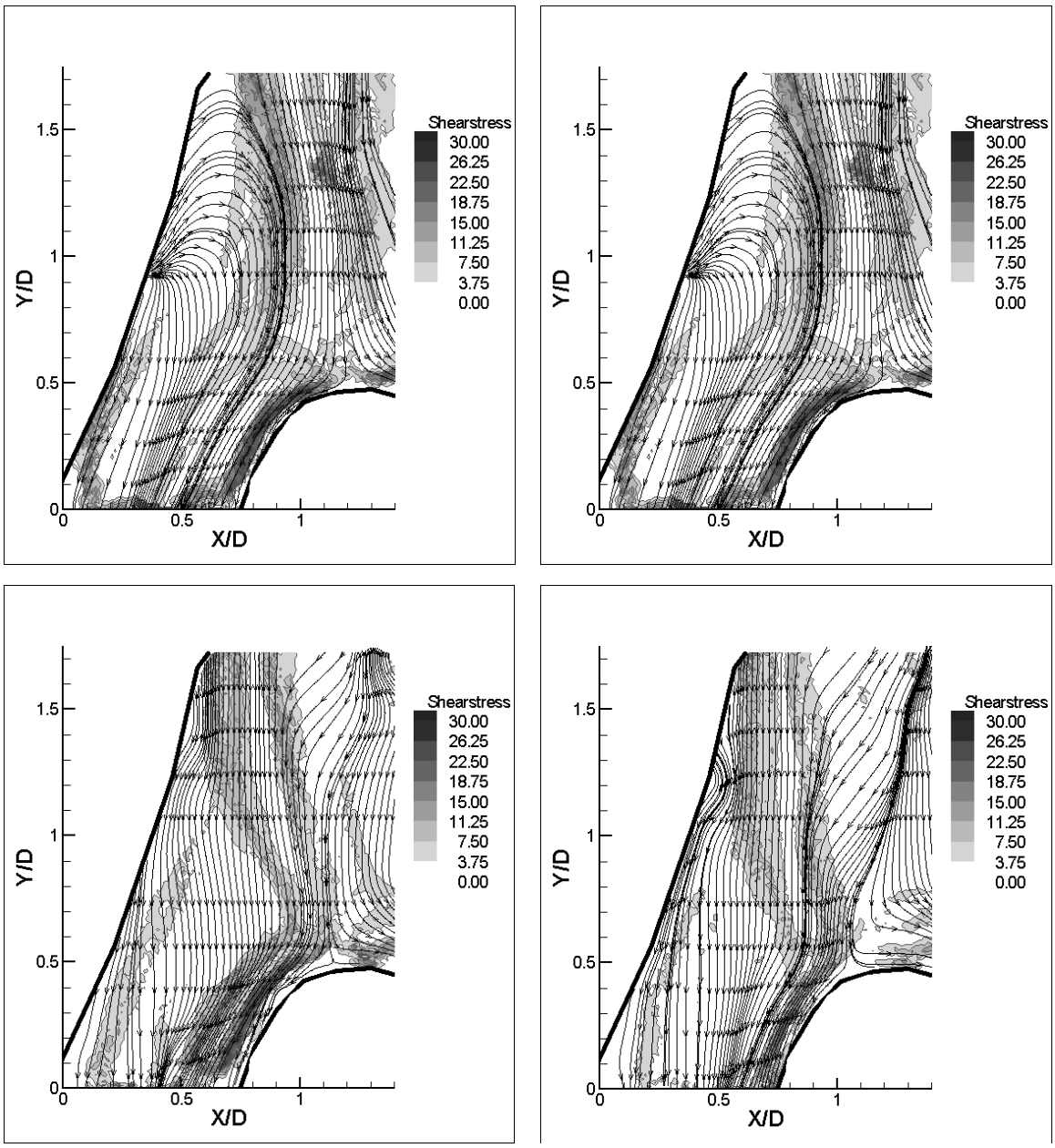

Figure 2.17: Instantaneous flow images illustrating flow conditions during declaration phase of the cycle for case6. (a) Flow is beginning to decelerate (top left). (b) Flow begins to decelerate more and form a separation region (top right). (c) Second separation begins to roll into a spiral motion confirming the occurrence of pinch-off (bottom left). (d) Second separation region is shown to have rolled into a small vortex with its center position at X/D = 0.45, Y/D = 1.2 (bottom right).

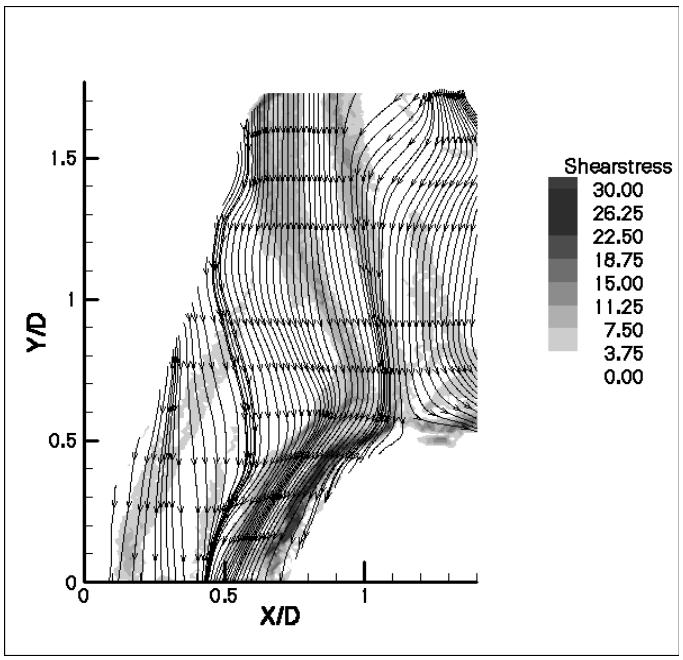

Figure 2.18: Instantaneous flow image illustrating the instant a second vortex is observed, thus ceasing the production of vorticity.

2.5. Discussion

We investigated the effects of the Womersley and the Reynolds numbers in a symmetric compliant bifurcation under pulsatile flow conditions. In order to obtain both high spatial and temporal resolution, we examined the flow behavior using time-resolve Digital Particle Image Velocimetry (DPIV). As expected, no flow disturbances existed during high systole. As flow decelerated (early diastole), the adverse pressure gradient induced flow separation and creation of vortical structures in the vicinity of the bifurcation apex. Moreover, the results showed that the formation of vortices is governed by a characteristic dimensionless time-scale ($U_m t/D*Re$), which we have referred to the vortex formation number. When the vortex formation number is approximately 0.01, the maximum amount of vorticity which the vortex can withhold is attained.

The vortex formation number for case 1 was measured to be 0.0057 occurring at a t* value of 0.488. Since no saddle points (or additional vortices) were observed, the formed vortex was assumed not be saturated. This same phenomenon also occurred for case 4, where the mean Reynolds number of the flow was the same as case 1, with a higher Womersley parameter. As the Reynolds number was increased from 80 to 280

(case 2 and 5), both saddle points and additional vortices were observed. This illustrates that by increasing Reynolds number, the vorticity generated increased to saturate the formed vortex and to initiate additional vortices. As Reynolds number was increased from 280 to 380, we observe again the existence of additional vortices, indicating saturation of the vortex has occurred. We note that the t* value for case 280 (case 2) and 380 (case 3) for a Womersley parameter of 8.5 decreased from 0.404 to 0.378. This demonstrates that the developed vortex saturated faster as the Reynolds number was increased, as expected. Also, for the higher Womersley parameter of 10.5, a slight decrease in the t* value was also occurred as the Reynolds number was increased from 280 (case 5) to 380 (case 6).

The location of flow separation and vortical structures has been clinically significant in vascular diseases. Regions of separation are associated with high wall shear stress gradient (WSSG) occurring at both the separation and reattachment point and very low wall shear stress (WSS). Endothelial cells (ECs) which align the blood vessels and serve as the protective layer are very susceptible to the shear forces exerted by the flow. It has been shown that in disturbed flow, both the orientation and shape of endothelial cells are changed due to the abnormal shear level detected by the cells, creating gaps in their uniformity. Scientist believes that these gaps may serve as the initiation point of the atherosclerosis process, the build of plaque in the vascular system. ECs serve as a bridge for blood elements to be transported from the blood stream to the smooth muscle cells, which are directly beneath the layer of ECs. When excess amount of low-density lipoproteins (LDL) are delivered to the smooth muscle cells, the intima thickens, increasing the probability of severe case stenosis, a decrease in the vessel diameter. The excess amount of LDL occurs as ECs are not able to perform their normal function

Flow separation and the existence of vortical structures have also shown to play a role in thrombus formation. A thrombus refers to a clot formed in the cardiovascular systems to prevent excess bleeding during external clots, or to prevent internal bleeding during injuries. Platelets, cell fragments that circulate freely in the vascular system, play an important role in thrombus formation. In their inactivated phase, they neither adhere to surfaces nor aggregate (adhere to themselves). As injury occurs in the vascular system, platelets begin to become activated, resulting in adhesion to the

subendothelium and adhesion to other platelets, resulting in a formation of a plug. Danger arises when platelets continue to aggregate leading to narrowing of the vessel lumen. Part of the thrombus may be detached and travel downstream until coming to rest in a small diameter vessel, blocking blood flow to vital tissue and organs.

Previous researchers have shown that platelets can also be activated when exposed to very high shear stress, or prolonged amounts of shear stress, as in circulation regions. In the carotid bifurcations, platelets begin to adhere to atherosclerotic plaques, increasing the severity of the stenosis, but more important, increasing the chance of an emboli; a broken piece of the thrombus. Previous studies have also shown that ADP release from sheared red blood cells enable platelets to adhere to surfaces and other platelets more rapidly (Bonnefoy et al. 2000; Plow and Marguerie, 1980). Taha et al. showed that the release of ADP from sheared red blood cells had a greater contribution to platelet adhesion, and platelet aggregation than the platelet themselves. Vortex formation dictates both in-flow and wall shear values and contribute directly to both shear stress sensed by the red blood cells and shear stress values occurring at vessel walls.

In the future, we will be looking to find similar relationships between formation of coherent vortices and any characteristic dimensionless time-scale for vascular bifurcation geometries. We also would like to investigate how the strength of a vortex affects blood elements, particularly blood platelets and red blood cells. Particular interest will lie upon red blood cells releasing ADP under high shear, blood platelets being triggered due to exposure to shear stress, and the aggregation and adhesion to surface of platelets in vortical flow. Temporal behavior of blood elements under abnormal physiological conditions may provide valuable information in the prevention of thrombosis.

Chapter 3 Conclusion

3.1. Stent Compliance

A high temporal and spatial resolution time-resolved DPIV system was used to explore the effects of stent compliance. Two specific phases that correspond to the unstable part of the pulsatile cycle most susceptible to disturbances created by the compliance mismatch were investigated. Our results revealed that flow induced disturbances and vortical structures were dependent on the compliance mismatch. Specifically, both the resident-time and the size of the ring vortex (two counter-rotating vortices) in the more compliant SMART stent were 50% less compared to the rigid cylinder stent. These results indicate that mechanical properties (compliance mismatch) directly affect resident time of blood, promotes platelet attachment, and alter normal physiologic shear stresses on endothelial cells, which could lead to failure of stents. Also noted is the three-dimensional characteristic of the flow associated with the ring vortex and its interaction with the walls. These flow patterns indicate that compliance mismatch causes flow in a vessel to depart from the classical paradigm of axisymmetric Womersley flow. The results of this effort improve our understanding of the intrinsic relationship between fluid mechanics and the cause of high rate failures in implanted stents, demonstrating the importance of mechanical properties for stent or other interventional therapies. Moreover, due to the enhanced spatial and temporal resolution, these results will support the validation and development of reliable and accurate computational models.

3.2. Symmetric Bifurcation

The effects of both Reynolds number and Womersley number were investigated in a symmetric compliant bifurcation under pulsatile flow conditions. During the deceleration part of the cycle, flow disturbances and vortical structures were observed in all cases. Moreover, the vortical structures were governed by a characteristic dimensionless time-scale associated with the inertia of the unsteady flow. When the vortex formation number (dimensionless time-scale) was approximately 0.01, the created vortex was endowed with the maximum amount of vorticity that was generated on the vessel walls. This was evident by the existence of saddle points in the flow field

that notified the structure of additional vortices. Vortical structures in the vascular system provide conditions that favor atherosclerosis. Separation and reattachment points of a separation region have shown to be associated with sites of atherogenesis. Understanding how separation regions are developed, and what parameters affect their structures may help in prevention of atherosclerosis and development of more intelligent implants.

References

[1] Babapulle, M., N., Eisenberg, M., J., 2002, "Coated Stents for the Prevention of Restenosis: Part II", Circulation, 2002, **106,** pp. 2800-5**.**

[2] Berry, J., L., Moore, J., E., Newman, V., S., Routh, W., D., 1997, "In vitro flow visualization in stented arterial segments", Journal of Vascular Investigation, **3**, pp. 63-68.

[3] Rachev, A, Manoach, E., Berry, J., L., Moore, J., E., 2000, "Model of Stress Induced Remodeling of Vessel Segments Adjacent to Stents and Artery/Graft Anastomoses. Journal of Theoretical Biology, **206(3)**, pp. 429-443.

[4] Rolland, P., H., Charifi, A-B., Verrier, Bodard, H., Friggi, A., Piquet, P., Moulin, G., Bartoli, J-M., 1999, "Hemodynamics and Wall Mechanics After Stent Placement in

Swine Iliac Arteries: Comparative Results From Six Stent Designs", Radiology, **213,** pp. 229-246.

[5] Berry J., L., Santamarina, A., Moore., J., E., Roychowdhury, S., Routh, W. D., 2000, "Experimental and Computational Flow Evaluation of Coronary Stents", Annals of Biomedical Engineering, **28,** pp. 386-398.

[6] Rogers, C., Edelman, E., R., 1995, "Endovascular Stent Design Dictates Experimental Restenosis and Thrombosis", Circulation, **91**, pp. 2995-3001.

[7] Tominaga, R., Emoto, H., Kambic, H., E., Harasake, H., Sutton, C., Hollman, J., 1992, "Effect of Design Geometry of Intravascular Endoprostheses on Stenosis Rate in Normal Rabbits", Am Heart J, **123**, pp. 21-28.

[8] Kastrati, A., Mehilli, J., Dirschinger, J., Dotzer, F., Schuhlen, H., Neumann, F., J., Fleckenstein, M., Pfafferott, C., Seyfarth, M., Schomig, A., 2001, "Intracoronary Stenting and Angiographic Results : Strut Thickness Effect on Restenosis Outcome (ISAR-STEREO) Trial", Circulation, **103**, pp. 2816-2821.

[9] Moore, J., E., Xu, C., Glagov, S., Zarins, C., K., Ku, D., N., 1994,"Fluid Wall Shear Stress Measurements in a Model of the Human Abdominal Aorta: Oscillatory Behavior, the Relationship to Atherosclerosis", Atherosclerosis, **110**, pp. 225-240.

[10] Ku D., N., Giddens, D., P., Zarins, C., R., Glagov, S., 1985, "Pulsatile Flow and Atherosclerosis in the Human Carotid Bifurcation: Positive Correlation Between

Plaque Localization and Low and Oscillating Shear Stress", Arteriosclerosis, **5**, pp. 293-302.

[11] He, X., Ku, D., N., 1996, "Pulsatile Flow in the Human Left Coronary Artery Bifurcation: Average Conditions", Journal of Biomechanical Engineering, **118**, pp. 74-82.

[12] Schajer, G., S., Roy, G., Flaman, M., T., 1996, "Hole-Drilling and Ring-Core Methods", The Fairmount Press Inc., Libum, GA, pp. 5-34.

[13] Abbott, W., M., Megerman, J., Hasson., J., E., L'Italien, G., Warnock, D., F., 1987, "Effect of Compliance Mismatch on Vascular Graft Patency", Journal Vascular Surgery, **5**, pp. 376-382.

[14] Stewart, S., F., C., Lyman D., J., 1992, "Effects of a Vascular Graft/Natural Artery Compliance Mismatch on Pulsatile Flow", J. Biomechanics, **25**, pp. 297-310.

[15] Rhee, K., Tarbell, J., M., 1994, "A Study of the Wall Shear Rate Distribution Near the End-to-End Anastomosis of a Rigid Graft and Compliant Artery", J. Biomechanics, **27**, pp. 329-338.

[16] LoGerfo, F., W., Quist, W., C., Nowak, M., D., Cranshaw, H., M., Haudenschild, C., C., 1983, "Downstream Anastomotic Hyperplasia: A Mechanism Failure in Dacron Arterial Grafts", Arch Surg, **197**, pp. 479-483.

[17] Cantelmo, N., L., Quist, W., C., LoGerfo, F., W., 1989, "Quantitative Analysis of Anastomotic Intimal Hyperplasia in Paired Dacron and PTFE Grafts", J. Cardiovasc Surg, **30**, pp. 910-915.

[18] Scarano, F., and Rieuthmuller, M.L., 1999, "Iterative Multigrid Approach in PIV Image Processing with Discrete Window Offset", Exp. In Fluids, **26**, pp. 513-523.

[19] Wereley, S., T., Meinhart, C., D., 2001, "Second-Order Accurate Particle Image Velocimetry", Experiments in Fluids, **31**, pp. 258-268.

[20] Mcdonald, D., A., 1974, "*Blood Flow in Arteries",* Williams & Wilkins, Baltimore, MD.

[21] Zamir, M., 2000, "*The Physics of Pulsatile Flow",* Springer-Verlag, New York.

[22] Chiu, J., J., Wang, D., L., Chien, S., Skalak, R., Usami, S., 1998,"Effects of Disturbed Flow on Endothelial Cells", J. of Biomechanical Engineering, **120**, pp. 2-7.

[23] Jour L-D, Berger S.A. 1998, "Numerical simulation of the flow in the carotid bifurcation", Theoretical and Computational Fluid Dynamics. **10**, pp. 239-248.

[24] Nazemi M., Kleinstreuer C. 1989, "Analysis of particle trajectories in aortic artery bifurcation with stenosis", Journal of Biomechanical Engineering, **111**, pp. 311-315.

[25] Zhao S.Z., Xu X.Y., Collins M.W., Stanton A.V., Hughes A.D., Thom S.A. 1999, "Flow in carotid bifurcations: effect of the superior thyroid artery", Medical Engineering and Physics, **21,** pp. 207-214.

[26] Rindt C.C.M., Steenhoven A.A. 1996, "Unsteady flow in a rigid 3-d model of the carotid artery bifurcation", Journal of Biomechanical Engineering, **118**, pp. 90-96.

[27] Lorthois S., Lagree P-Y., Marc-Vergnes J-P., Cassot F. 2000, "Maximal wall shear stress in arterial stenoses: application to the internal carotid arteries", Journal of Biomechanical Engineering, **122**, pp. 661-666.

[28] Perktold K., Hofer M., Rappitsch G., Loew M., Kuban B.D., Friedman M.H. 1998, "Validated computation of physiologic flow in a realistic coronary artery branch", Journal of Biomechanics, **31**, pp. 217-228.

[29] Gijsen F.J.H., Vosse F.N., Janssen J.D. 1999, "The influence of non-Newtonian properties of blood on the flow in large arteries: steady flow in a carotid bifurcation model", Journal of Biomechanics, **32**, pp. 601-608.

[30] Carr R.T., Kotha S.L. 1995, "Separation surfaces for laminar flow in branching tubes-effect of Reynolds number and geometry", Journal of Biomechanical Engineering, **117**, pp. 442-447.

[31] Lee C.S., Tarbell J. M. 1997, "Wall shear rate distribution in an abdominal aortic bifurcation model: effects of vessel compliance and phase angle between pressure and flow waveforms", Journal of Biomechanical Engineering, **119**, pp. 333-342

[32] Palmen D.E., Van De Vosse F.N., Janssen J.D., Van Dongen M. E. H. 1994, "Analysis of the flow in stenosed carotid artery bifurcation models-hydrogen-bubble visualization", Journal of Biomechanics, **27**, pp. 581-590

[33] Gharib M., Rambod E., Shariff K., 1998. "A Universal Time Scale for Vortex Ring Formation," J. Fluid Mech., **360**. pp. 121-140.

Vita

Saami K. Yazdani was born on April 16, 1979 in Tallahassee Florida to Ali and Faridah Yazdani. At the age of 4, he moved to Dubai, which is located in the United Arab Emirates. Two years later he moved to Shiraz (Iran) where he lived with his Father, Brother, Aunt, and grandparents. After finishing fourth grade, he moved to Houston. After two years in Houston, he went back to Shiraz for another two years. Beginning of high school he moved to Fairfax Virginia where at the time his Father and Brother were living. He Graduated From Robinson Secondary School in 1997. He ran track his last three years of high school where he was one of the top 300 IM hurdlers in his region. He attended Virginia Tech in the fall of 1997 and graduated with a B.S. degree in Engineering Science and Mechanics. He met many great friends that he is still in contact with. Fortunately for Saami, most of his friends are still in school and have yet to leave to start their careers. Saami is currently pursuing his PhD in Biomedical Engineering at Wake Forest University School of Medicine. His main focus lies in cardiovascular biomechanics, specifically cardiovascular stents. Saami's interest lie in watching sports, especially college football and European soccer, playing tennis, and spending time at the gym. Saami inspires to become a great High School Football coach one day and to be able to watch his sons win national championships.